DEFORMATION MECHANISMS ACCOMMODATING PROGRESSIVE SIMPLE SHEAR THRUSTING OF QUARTZITE AND METACARBONATE IN THE SOUTHWESTERN ESPINHAÇO RANGE, BRAZIL

Rhander Taufner[a*1], Leonardo Lagoeiro[a], Carolina Cavalcante[a,b], Paola Barbosa[c], Camila Santos Silveira[a]

[a] *Departamento de Geologia, Universidade Federal do Paraná, Av. Cel. Francisco Heráclito dos Santos, s/n, Centro Politécnico, 81531-980, Curitiba, PR, Brazil*

[b] *UiT-The Arctic University of Norway, Postbooks 6050 Langnes, N-9037 Tromsø, Norway*

[c] *Instituto de Geociências, Universidade de Brasília, Campus Universitário Darcy Ribeiro ICC – Ala Central – CEP 70910-900, Brasília, DF, Brazil*

*Corresponding author: rhander.altoe@gmail.com

Abstract

The accommodation of low-temperature ductile deformation in foreland fold-and-thrust belts are often described in terms of outcrop-based geometric analysis, but microtextural observations are also important, as they relate stress, strain, fluids and temperature and thus the rheology in the peripheral part of the orogen. Such microtextural observations are lacking from the foreland part of the Araçuaí orogen in Brazil, and are here investigated through EBSD-based textural analysis of quartzites and metacarbonate samples from the southwestern Espinhaço Range. The quartzites overthrust the metacarbonates, and deform solely by the activation of dissolution-precipitation creep, whereas the metacarbonates show a much greater variety of deformation mechanisms that closely relate to grain-size, composition and strain, in the long (low-angle) and short (steep) limbs of shear-related folds. The metacarbonates show a centimeter-scale alternation of coarse-grained domains of calcite and quartz, and fine-grained domains of a mix of phases (calcite, dolomite, phyllosilicates, quartz, and apatite). In the strongly sheared long limbs, coarse calcite

[1] Current address: Instituto de Geociências, Universidade de Brasília, Campus Universitário Darcy Ribeiro ICC - Brasília DF

was deformed by dislocation creep with slip on (c)<a>, whereas fine calcite displays evidence of oriented dissolution-precipitation creep, with both cases displaying <c> axis orientations consistent with the top-to-the-west thrusting. Coarse calcite shows evidence of recovery by subgrain rotation and grain boundary migration. Coarse-grained calcite in the short limbs was deformed by dislocation creep, assisted by twin boundary migration recrystallization with twinning on {e}, indicating simple shear-dominated deformation. In contrast, fine-grained calcite was deformed by fluid-assisted grain boundary sliding. Dissolution-precipitation in both short and long limbs produced random textures, with the exception of coarse quartz in the short limbs, where dissolution-precipitation creep led to <c> axis orientation parallel to X. This study demonstrates that the foreland thrust zone of the Araçuaí orogen underwent consistent W-directed progressive thrusting, and that this deformation produced a wide variety of texture types in the metacarbonates while a simpler structural and textural pattern developed in adjacent quartzitic metasediments.

Keywords: Araçuaí orogen, quartz, calcite, dissolution-precipitation creep, dislocation creep, EBSD.

1 Introduction

Calcite and quartz are important rock-forming minerals in the upper crust that often record intense ductile deformation and strain localization along shear zones in orogenic belts. Microstructural and textural analyses (texture is the term used here to refer to crystallographic preferred orientation - CPO) in experimental and natural ductile shear zones have evaluated the rheological behavior of carbonate- and quartz-rich rocks during deformation (e.g. Barnhoorn et al., 2004; Bestmann et al., 2000; Busch and Van der Pluijm, 1995; De Bresser and Spiers, 1997; Dietrich and Song, 1984; Faghih and Soleimani, 2015; Van der Pluijm, 1991), in terms of deformation

54 mechanisms and development of CPO data. These studies suggest that a wide range
55 of deformation mechanisms can simultaneously be activated to accommodate
56 deformation, and the presence of CPO has been linked to mechanical and anisotropic
57 properties of the aggregate (e.g. Padrón-Navarta et al., 2012; Pearce and Wheeler,
58 2001; Shaocheng and Mainprice, 1988; Tommasi and Vauchez, 2015 and references
59 therein).

60 Grain size reduction due to dynamic recrystallization in calcite and quartz
61 aggregates occurs at temperatures above 150 ˚C (Kennedy and White, 2001; Molli et
62 al., 2010, 2011; Bauer et al., 2018) and ~300 ˚C (Stipp et al., 2002), respectively,
63 which may lead to strain localization as a result of changes from the dominant
64 deformation mechanism, e.g., dislocation creep to diffusion creep (Schmid et al., 1977;
65 Etheridge and Wilkie, 1979; Behrmann, 1985; Rutter, 1995; Bestmann et al., 2000;
66 Bestmann and Prior, 2003; Barnhoorn et al., 2004; Barber et al., 2007; Rogowitz et
67 al., 2016). Under such greenschist facies temperature conditions, quartz aggregates
68 typically deform by dislocation creep, in which strain is accommodated by glide on
69 active slip systems producing several texture patterns, depending on the strain,
70 temperature (e.g., Tullis, 1990; Stipp et al., 2002) and strain rate (Kilian and
71 Heilbronner, 2017). For experimentally deformed calcareous rocks, Schmid et al.
72 (1987) propose a variety of deformation conditions at which calcite changes texture
73 and microstructure with evolving deformation.

74 Weak to random CPO of the mineral aggregate have sometimes been related
75 to dissolution-precipitation creep (e.g. Menegon et al., 2008). However, deformation
76 in a fluid-rich environment at the upper crust may also develop a CPO, which is
77 commonly associated with stress-controlled dissolution-precipitation creep
78 mechanisms (Hippertt, 1994; Takeshita and Hara, 1998; Lagoeiro et al., 2003). As

fluids are usually present during dynamic metamorphism (e.g. Philpotts and Ague, 2009; Putnis and Austrheim, 2010), the role of dissolution-precipitation creep and temperature-dependent dislocation glide as the dominant deformation mechanisms is an interesting issue that needs to be further explored (Bestmann et al., 2004; Menegon et al., 2008; Wassmann and Stöckhert, 2013; Wintsch et al., 2005).

In this work, we explore the microscale response to thrusting in the foreland section of the Araçuaí orogen. Calcite and quartz are important constituents of the deformed metasedimentary rocks in this section, as both quartzites of the Espinhaço Supergroup and metacarbonates of the Bambuí Group record intense ductile low-temperature deformation. Although the studied area has been subjected to several macroscale structural studies (e.g. Bacellar, 1989; Magalhães, 1989; Uhlein, 1991), texture analyses at the microscale, essential to explore deformation mechanisms and strain accumulation in relation to thermal conditions and rheology, are lacking in these rocks. Thus, this contribution aims: (1) to provide a description of the microstructures and textures of the quartzite from the Espinhaço Supergroup and metacarbonate from the Bambuí Group, focusing on calcite and quartz; and (2) to investigate the deformation mechanisms, i.e. the way these rocks accommodate the imposed deformation, in order to understand the mechanical response of rheologically weak metacarbonates bounded by strong quartzites in a greenschist facies thrusting environment.

2 Geological Setting

The study area is located in the western foreland of the Araçuaí orogenic belt, with the much hotter external zone (hinterland) of the Araçuaí belt located to the east. In our study area, quartzites of the Espinhaço Supergroup (1.8-1.0 Ga; e.g. Chemale Jr. et al., 2012; Guadagnin and Chemale Jr., 2015; Santos et al., 2013) tectonically

overlay metacarbonates of the Bambuí Group (635-560 Ma; e.g. Moreira et al., 2020; Paula-Santos et al., 2015) that were deposited on the São Francisco Craton (SF; Fig. 1) before and during the Neoproterozoic orogenic evolution. These rocks are affected by regional thrusts (e.g. Herrgesell and Pflug, 1986), with a mylonitic foliation dipping moderately to the ENE. The quartzites define a roughly N-S trending mountain range, the Espinhaço Range, and are thrusted on top of metacarbonates of the younger Bambuí Group of the São Francisco Basin (Figs. 1, 2).

The Espinhaço Supergroup is a ca. 5 km thick unit (Marshak and Alkmim, 1989) composed of metasandstone and metaconglomerate with intercalated phyllites, and with lenses of marble in its uppermost metapelite section (e.g. Almeida and Litwinski, 1984; Martins-Neto et al., 2001), deposited in an intracontinental foreland basin (e.g. Guadagnin and Chemale Jr., 2015). At the western edge of the Espinhaço Range, the quartzites of the Espinhaço Supergroup form a high escarpment, at the base of which carbonate rocks of the Bambuí Group are intensely sheared and folded (Marshak and Alkmim, 1989). From geological mapping in the Espinhaço Range area, Marshak and Alkmim (1989) suggest reactivation and inversion of pre-existing detachment fault separating the sheared Bambuí limestones from deformed overlying Espinhaço quartzites. The Espinhaço Supergroup defines a west-vergent fold-and-thrust belt (e.g. Almeida Abreu et al., 1986; Hartmann, 1987; Herrgesell and Pflug, 1986; Uhlein et al., 1991) with rocks containing white mica, quartz, kyanite, chlorite, chloritoid and opaque minerals (Magalhães, 1989), a mineral assemblage consistent with lower greenschist facies conditions (300 – 400 °C; Winkler, 1979).

The Bambuí Group lies west of the Espinhaço Range (Figs. 1, 2) and comprises recrystallized dolomite mudstone, crystalline dolomite limestone and impure crystalline limestone (Tuller et al., 2010), deposited in a foreland-type basin.

Deformation in the Bambuí Group has been attributed to the presence of open, upright to inclined folds with axial planar slaty cleavage, and to shearing. The E-W stretching mineral lineation and asymmetric structures indicate westwards tectonic transport (Bacellar, 1989; Marshak and Alkmim, 1989). Occasionally, the original bedding has been transposed into a mylonitic foliation which is axial planar to the recumbent isoclinal folds (Marshak and Alkmim, 1989).

Fossil marker from the lower portion of the Bambuí Group suggests deposition between 550 and 542 Ma (Warren et al., 2014), while detrital zircons from the middle and upper portions indicate deposition between 650 and 616 Ma (Pimentel et al., 2011). Deformation in both quartzites and metacarbonates has been attributed to a progressive deformation related to the 630-530 Ma Araçuaí orogeny (Alkmim et al., 2017). Illite K-Ar ages ranging from 645 to 603 ± 9Ma from the Espinhaço Supergroup interpreted as the timing of deformation and metamorphism (Süssenberger et al., 2014), suggest that deformation started in the early Ediacaran, evidencing uncertainties in the literature data. Regardless of timing and, the regional deformation of both Espinhaço and Bambuí conforms with east-west contractional deformation (Alkmim et al., 2006) in response to convergent motions between the SF and Congo cratons (e.g. Cavalcante et al., 2019 and references therein).

3 Sampling and field observations

Three quartzite samples (PSC 001, 002, and 003) from the Espinhaço Supergroup and thirteen metacarbonate samples (PSC 101-106, and PSC 201-207) from the Bambuí Group were collected in three localities along a section perpendicular to the thrusts (Figs. 1, 2). These localities were selected for two reasons: 1) they are well-exposed and representative outcrops of deformed rocks from these two units; and 2) they come from localities at steep and low-angle limbs, interpreted as short and

154 long limbs of a large-scale shear-related fold (Fig. 3a). Sampling of these two limbs
155 was also done because the long limbs appeared to be more strained.

156 The quartzites display a well-developed cleavage defined by concentrations of
157 phyllosilicates and quartz dipping between 15 and 60° mainly to ENE (Fig. 1). The
158 lineation, which is characterized by the preferred orientation of phyllosilicates, plunges
159 ~30° to NE. A macroscopically striking feature of the quartzite is the presence of
160 asymmetric shear-band type boudins of quartz vein and phyllosilicates, indicating top-
161 to-the-west sense of shear (Figs. 3a, 4a). Together with the NE-plunging mineral
162 lineation, this implies tectonic transport onto the São Francisco craton.

163 Excellent exposures of metacarbonates are found in two quarries. The eastern
164 quarry (PSC 105; Fig. 1) is located roughly 50-100 m from the thrust contact with the
165 quartzite unit, at the base of the Espinhaço Range, where the older quartzite
166 overthrusts the younger metacarbonate. The western quarry (PSC 204; Fig. 1) lies
167 roughly 4 km away from the thrust zone.

168 Metacarbonate rocks from the east quarry (PSC 105 locality in Fig. 1 and short
169 limbs in Fig. 3a) display asymmetrically folded foliation with limbs dipping ENE and
170 WNW and hinge line plunging ~ 20° N (Fig. 1). The foliation is marked by alternating
171 centimeter-scale dark and light gray layers (which represents the fine-grained domain
172 or matrix, as described later) that likely are reworked and transposed depositional
173 layering (Fig. 2 and 4b-d). Millimeter- to centimeter-scale white quartz-calcite veins
174 (coarse-grained domain) that are parallel or occasionally cut the layering occur
175 frequently (Fig. 4c). Some veins are folded while others are associated with cm-thick
176 shear zones that are axial planar to overturned folds dipping ~70° to ENE (Figs. 4d
177 and stereoplot for PSC 105 in Fig. 1). Non-cylindrical plunging inclined isoclinal folds

178 (Fig. 2) and possible sheath folds (Fig. 4b) are the dominant structures found in these
179 rocks.

180 The metacarbonate rocks located at the western quarry (PSC 204 in Fig. 1 and
181 long limbs in Fig. 3a) have a completely transposed W-dipping mylonitic foliation (Fig.
182 4e). Calcite and quartz layers are folded (intraformational recumbent fold; Fig. 2
183 sample PSC 204) in a way that their axial planes coincide with the mylonitic foliation
184 and their hinges are rotated towards the shear direction, parallel to the mineral
185 lineation. The mineral lineation plunges 20-30° to the west, parallel to the fold hinges
186 (Fig.1). It is defined by the alignment of phyllosilicates and elongated calcite and quartz
187 on the west-dipping foliation.

188 **4 Methods**

189 We used optical microscopy and electron backscatter diffraction technique
190 (EBSD) by means of the scanning electron microscope (SEM) for microstructural and
191 textural analysis. Samples were cut parallel to the lineation and perpendicular to the
192 foliation (XZ-plane of the finite strain ellipsoid). Thin sections were polished in a
193 conventional way and finished with a colloidal silica lapping for thirty minutes. EBSD
194 data were acquired using a MIRA 3RM SCAN-SEM in the Lactec Institute at the
195 Federal University of Paraná, Brazil. An Oxford Instruments/HKL Channel 5 software
196 was used for data treatment. SEM conditions were set as following: thin sections were
197 placed in the scanning electron microscope (SEM) chamber at a 20° tilt angle to the
198 electron beam (70° to the horizontal surface) and the rock lineation parallel to the SEM
199 X-axis. EBSD patterns were acquired at an acceleration voltage of 15 kV, and a
200 working distance and beam current of 11 mm and 18 nA, respectively. A series of
201 high-resolution maps were collected using a step size of 3 μm. Data were noise
202 reduced, which included removal of pixels different in orientation relative to their

surroundings 8 pixels and extrapolation of zero solutions surrounded by 6 neighbor-pixels of the same phase. The fabric strength (M-index; Skemer et al., 2005 and the J-index; Bunge, 1982) shown in the pole figures was calculated using the MTEX toolbox 5.1.1 using an optimal Gaussian Half Width based on the population of grain in the sample.

The textural analysis results for quartz and calcite are presented in Figures 3b-c, 9-13. Directions of c (0001), a < -12-10 >, m {10-10}, r {10-11} and z {01-11} for quartz, and c (0001), a < -12-10 >, e {-1018}, r {10-14} and f {-1012} for calcite were derived from the orientation distribution function (after Bunge, 1982), and plotted as equal area upper hemisphere projections. Moreover, neighbor-pair and random-pair misorientation angle distributions are represented together with the calculated theoretical misorientation angle distribution for trigonal crystal symmetry. Grains were detected using an angle of 10º or higher whereas subgrain boundaries were classified as having 2-10º of misorientation between neighboring parts of a grain. We display misorientation angles in misorientation angle distribution histograms where the relative frequency of occurrence is plotted against the angle of misorientation as measured in degrees. In the histograms, misorientation angles are binned into 5° increments, and the minimum misorientation angle is 3° to minimize errors associated with measurement at very low angles.

Additionally, qualitative chemical characterization of metacarbonate samples were performed using the energy-dispersive X-ray spectroscopy (EDS) under a QEMScan to examine variation in the mineral composition between fine-grained and coarse-grained microstructural domains.

5 Microstructures

The following microstructural descriptions will proceed from the quartzites to the metacarbonates (Figs. 5-8), highlighting features in quartz and calcite aggregates, the dominant mineral phases.

5.1 Quartzite

The foliation in the quartzite is defined by dark iron-oxide rich stripes, by the alignment of white micas and the long axis of elongated quartz and feldspar grains (Fig. 5a). Relatively large grains (200 – 400 μm) of feldspar and quartz in a fine-grained matrix of quartz (mean 22 μm in size; Fig. 6a), feldspar and flakes of muscovite form a sort of anastomosing microscale pattern (Figs. 5a-b).

Quartz grains generally exhibit patchy undulose extinction with minor subgrains (Fig. 5c), and well-developed sigma-type pressure shadows of newly-precipitated quartz, together with white mica beard parallel to the maximum extension direction (Fig. 5d). Quartz grains occasionally exhibit a ‘fish-shaped’ geometry with overgrowths (Figs. 5d-e). Both sigma-type pressure shadow and fish-shaped features indicate top to the west sense of shear, in agreement with the kinematics suggested by the asymmetric boudins and S-C fabrics observed in the field (Figs. 3a, 4a). Feldspar commonly shows tapered twins, with the foliation wrapping around the grains (Fig. 5f). Quartz and feldspar grains in the matrix are flattened and interconnected with flakes of muscovite showing irregular edges.

5.2 Metacarbonates

Two domains in the metacarbonates were distinguished: (1) a coarse-grained domain (CGD) formed by calcite and quartz; and (2) a fine-grained domain comprising calcite, dolomite, phyllosilicates, quartz, feldspar and apatite (FGD; Fig. 7). Thickness

of both domains varies from a few micrometers to up to ~50 centimeters. The alternating CGD and FGD defines the foliation at both macro- and microscale.

Coarse-grained domain (CGD)

The CGD comprises veins composed by calcite and quartz (Figs. 7a-b, 8a-d). In these domains, the calcite grain-size from both PSC 105 and PSC 204 samples averages 62 μm (Fig. 6b). Calcite- and quartz-rich domains occur parallel to the foliation (MF in Figs. 7b, 8c) and a grain shape preferred orientation is seen at ~40-60° from the foliation (SP in Fig 8c), consistent with top-to-the-W sense of shear. The density of calcite twins in sample PSC 105 (from short limbs of shear folds) is larger than in PSC 204 (from long limbs of shear folds), but their microfabrics are very similar. Most calcite grains exhibit serrated, lobate, and straight grain boundaries, locally developing triple junctions (Figs. 8a-b). Subgrains are similar in size to the recrystallized grains, based on a rough optical estimation. Coarser calcite grains in sample PSC 105 show undulose extinction with development of subgrains, and one or more well developed sets of bent or tapered twins with small new grains along twin bands (Fig. 8c). Calcite in sample PSC 204 is mostly twin free. Phylosillicates – illite, chlorite, muscovite and biotite – are widely spread and are oriented parallel to the foliation, defining a pressure solution cleavage. Quartz grains show lobate and bulbous boundaries, the latter being dominant (Figs. 8a, d). Overall, grains are inequant, ranging in size from 45 μm to 320 μm (mean 83 μm; Fig. 6c), locally showing a grain shape orientation (Fig. 8c-d) consistent with top-to-the-W sense of shear. The CGD are locally folded at the microscale (Fig. 8e).

Fine-grained domains (FGD)

Transition from CGD to FGD is sharp in all samples (Figs. 8e-f). The averaged grain size of calcite and quartz is 19 μm and 15 μm, respectively (Figs. 6d-e). These grains have a shape preferred orientation at ~40-60° from the foliation similar to those found for grains in the CGD (Figs. 8f-h), consistently suggesting top-to-the-W sense of shear. Overall, calcite, quartz and dolomite are strain-free, and minor twins occur in calcite grains. The amount of quartz is small (<4%; Fig. 7c), interphase grain boundaries are often straight to slightly curved, eventually forming triple junctions, and phyllosilicates are oriented parallel to the foliation.

6 EBSD-based textural analysis

6.1 Quartzite

Quartz

Quartz texture strength is weak in the quartzite (J-index = 1.05 and M-index = 0.003; Table 1), and shows a broad maxima distribution. The c-axis maxima define a great circle halfway between Y and Z (Figs. 9a-b). The <a> axes are at high angle to the X-direction. Maxima for m, r and z are faint (Figs. 9a-b).

Misorientation angles between neighbouring grains show a small deviation from a random distribution. A discreet peak appears at low angles (<10˚), likely related to the presence of subgrains, and an even more discreet peak can be observed in the range between 10˚ and 25˚ (Fig. 9c). On the other hand, a sharp peak for neighboring grains (grains with mutual interfaces) appears around 55˚. This might be attributed to the presence of Dauphiné twinning in quartz grains, as suggested by several authors (e.g. Lloyd, 2004; Pennacchioni et al., 2010; Wheeler et al., 2001).

6.2 Metacarbonates

Coarse-grained domains

297 In the CGD, calcite fabric intensity displays values of J-index ~ 2.2 and M-index
298 ranging from 0.02 to 0.08 for both samples (PSC 105, 204), while quartz has J-index
299 of ~ 1.3 and M-index between 0.01 and 0.03 (Figs. 10a, 11a; Table 1).

300 Poles to calcite c-planes from sample PSC 105 show two maxima, with the
301 strongest one oriented about 40˚ clockwise from the z-axis, and the weakest one close
302 to Z (Fig. 10a). <a> axes are rather distributed with a tendency to cluster around small
303 circles with broad angles. The rhombohedral planes also lack a well-defined
304 maximum. Rhombs {e} have poles asymmetrically distributed around the Z axis,
305 pointing to the direction of maximum shortening (Fig. 10a). A more disperse
306 distribution is found for poles to {r} and {f}, but weak maxima forming small circles can
307 be observed. It is worth to note that poles to those main crystallographic planes (c)
308 and {e} are parallel to the shortening direction, in the opposite direction of the shear
309 sense, or are oriented around the Z-axis (Fig. 10a). Calcite neighbor-pair
310 misorientation angle follows a rather random distribution, yet with small peaks at low
311 angle boundaries, at 30˚ and a sharper peak around 70-75˚ (Fig. 12a).

312 Quartz c-axes from sample PSC 105 are oriented close to the X-direction (Fig.
313 10a). a-axes form two maxima: one is concentrated halfway between Y and Z and
314 another close to Z. Rhomb planes show poles in a threefold configuration typical of
315 single crystal distribution (Fig. 10a). Misorientation angle distribution is similar to that
316 observed for quartz in the quartzitic unit (Fig. 9c). A small peak of neighbor-pair
317 misorientation occurs at low angle boundaries and another one around 55˚. The rest
318 of the distribution follows the curve of a random distribution (Fig. 12a).

319 Pole figures of sample PSC 204 display maxima of calcite c-axis both parallel
320 to Z and about 30˚ counterclockwise to Z (Fig. 11a). Poles to the e-planes present a
321 similar distribution, but with weaker maxima. The a-axes form maxima distributed

along a broad girdle inclined 30˚counterclockwise to the foliation (Fig. 11a). Poles to {r} tend to show a wider distribution with a slight tendency to concentrate in the NW and SE quadrants. Poles to {f} planes show a rather faint concentration in the center and at the NE and SW quadrants. Neighbor-pairs misorientation angle distribution displays peaks at 5˚, at 70-75˚ (Fig.13a), and a more discreet peak at 20 and 30˚.

Quartz c- and a-axes and m-, r- and z-planes in sample PSC 204 are diffuse, forming small concentrations (Fig. 11a). Misorientation angle distribution for random pairs tends to follow the theoretical curve, with distinct high peaks at low angles (<10˚) and high angles (20-45˚), whereas neighboring grains show peaks of misorientation angles at 30˚ and 55˚ (Fig. 13a).

Fine-grained domain

In the FGD, J-index for calcite ranges from 1.1 to 1.3, while M-index is 0.01 (Figs. 10b, 11b; Table 1). Quartz J-index ranges from 1.4 to 1.5 and M-index from 0.00 to 0.01 (Figs. 10b, 11b; Table 1). The highest fabric intensity values, for both calcite and quartz, are from sample PSC 204.

The c-axes of calcite grains in sample PSC 105 show a broad distribution around the Z-axis (Fig. 10b). Three main maxima occur as small circles, centered around a direction at 20˚ to Z, facing the maximum shortening direction. These preferred orientations of calcite fine grains are similar to those of the c-axes of calcite crystals of the coarser domains (Fig. 10a). Similarly, poles to e-planes have somewhat similar c-axis distribution patterns, although with a wider spreading throughout the periphery of the pole figures. Likewise, poles to {r} show even wider spreading with none visible maximum (Fig. 10b). The distributions of poles to {f} planes are still broader. The a-axes spread roughly around the center of the pole figure. Calcite

misorientation angle distribution fits well into the random distribution curve (Fig. 12b). However, discreet peaks appear for angles between 25-30˚ and around 70-75˚.

Quartz texture in sample PSC 105 is weak and axes are randomly distributed around the pole figure (Fig. 10b). However, a slight clustering of a-axes is observed close to the X-axis. The misorientation angle distribution for neighbor-grains shows peaks at 10˚ and 55-70˚ (Fig. 12b). However, this observation must be considered with care because of the lack of neighbor quartz grains (correlated grains), which may lead to biased peaks. Nevertheless, histograms for random pairs closely fit the theoretical curve (Fig. 12b)

The c-axes of calcite for sample PSC 204 form two small circles with concentrations at ~10˚ and ~35˚ counterclockwise to the Z-direction, toward the shear direction (Fig. 11b) and parallel to the grain shape orientation observed at the microscale (Fig. 8c). Poles to the {e} form a weak texture but follow the same pattern as the c-axes. Poles to {r} and {f} show a more diffuse texture while the a-axes form a broad girdle oriented roughly ~30˚ anticlockwise from the X-direction (Fig. 11b). Misorientation angles follow a random distribution with no distinct peaks, fitting well into the random curve of distribution (Fig. 13b). Quartz CPO for all crystallographic planes for sample PSC 204 show concentrations spread around the pole figure (Fig. 11b).

7 Discussion

The formation of the Araçuaí orogen during the Brasiliano event developed a foreland fold-and-thrust system that placed Paleoproterozoic quartzites of the Espinhaço Supergroup on top of the Neoproterozoic metacarbonates of the Bambuí Group, thus creating a stratigraphic inversion and sandwiched the metacarbonate

370 rocks (Fig. 2). In the study area, field observations suggest that the Brasiliano event
371 is characterized by a heterogeneous distribution of deformation typified by competent
372 layers of quartzites with boudin features and a well-defined NNW-SSE trending
373 cleavage, and incompetent layers of intensely folded carbonates with centimeter-scale
374 shear zones, sandwiched between the quartzite units (Figs. 1, 2, 3a, 4).

375 The heterogeneous deformation recorded in the metacarbonates produced
376 characteristic structures and crystallographic textures of shear-related rocks that we
377 generically define as metacarbonate mylonite. The coexistence of coarse-grained
378 domains, which consist of calcite and quartz veins, and fine-grained domains, which
379 contain a mix of phases such as calcite, dolomite, phyllosilicates, quartz, feldspar and
380 apatite (Fig. 7), can be partially a result of differences in composition. In the fine-
381 grained domain, the mix of phases could prevent mineral growth by pinning (e.g. Ebert
382 et al., 2008). Such a restriction on mineral growth is less likely in the coarse domains,
383 as it consists only of calcite and quartz and displays evidence of grain boundary
384 migration (Figs. 8a-b), which lead to grain growth. Strain recorded in the
385 metacarbonates from the western quarry (long limbs, sample PSC 204) resulted in a
386 more prominent mylonitic foliation with fold axis rotated into parallelism with the
387 mineral lineation (Figs 3a, 4e). Large-scale asymmetric folding occurred during the
388 progressive shearing, rotating early folds and forming a local overprinting axial planar
389 foliation (short limbs in the eastern quarry, sample PSC 105), as shown in Figure 3a.
390 Concerning texture development in general, the weak texture strength observed in all
391 rocks points out to widespread presence of dissolution-precipitation creep, fluid-
392 assisted grain boundary sliding and minor dislocation-creep mechanisms (Table 1).
393 We will address the activation of each mechanism in the following sections.

394 *7.1 Deformation mechanisms in the Espinhaço quartzites*

Dissolution-precipitation creep plays a major role in hydrous rocks deformed in the upper crust under low or non-metamorphic conditions (e.g. Gratier et al., 2013). Evidence for operation of this mechanism as observed within the asymmetric quartz vein boudins in the quartzites (Fig. 4a) are: the development of a pervasive foliation by muscovite alignment (Figs. 5a-b; e.g. Gray, 1978); oxide trails (Fig. 5a; e.g. Gray, 1978); pressure shadows, quartz overgrowth and mica beards around quartz and feldspar grains (Figs. 5d-f; e.g. Davis et al., 2011; Hippertt, 1994) and; the shape preferred orientation of quartz grains lacking a well-developed texture (Figs. 3c, 9; e.g. McPherren and Kuiper, 2013). Intracrystalline plasticity is only observed as undulose extinction and minor quartz subgrains (Fig. 5c).

Although textural development is often associated with intracrystalline plasticity, oriented crystallographic fabrics can also form during dissolution-precipitation creep (e.g. Hippertt, 1994; Takeshita and Hara, 1998; Lagoeiro et al., 2003). In our case, however, quartz c-axes in sample PSC 003 have weak preferred orientations and the lowest fabric index values of all samples (Figs. 3c, 9; Table 1), showing that precipitation did not lead to any significant crystallographic preferred orientation. This, together with the small peaks of mismatch angles between neighboring grains (<15°), indicating the presence of subgrains, and high peaks at ~60º, indicating the presence of Dauphiné twinning (Fig. 9c), suggest that the planar fabric of the quartzites is a shape preferred orientation resulting from the activation of dissolution-precipitation creep, accompanied by some dynamic recrystallization, and facilitated by Dauphiné twinning (e.g. Menegon et al., 2011).

7.2 Deformation mechanisms in coarse-grained metacarbonates

Evidence for some crystal-plastic deformation mechanisms is observed in both of the samples PSC 104 and PSC 205. Calcite texture in the long limb of shear folds

(sample PSC 204) shows widely distributed e-planes, suggesting that e-twinning alone did not account for most of the strain (Fig. 11a). This is evidenced by the moderate misorientation angle between neighbor grain pairs at 70-75º (Fig. 13a). Clustering of c-axes either normal to the foliation or at ~35° counterclockwise to Z, and a-axis girdle slightly inclined counterclockwise to the foliation (Figs. 3b, 11a), suggest activation of (c)<a> slip system. Such a slip system usually occurs at high finite strains and due to activation of dislocation creep deformation mechanisms (e.g. Barnhoorn et al., 2004, Vauchez et al., 2013). Additionally, the c-axis fabric is consistent with the top-to-the-W sense of shear during simple shear deformation. The lobate and straight calcite grain boundaries, and the presence of recrystallized grains similar in size to the subgrains indicate grain boundary migration and subgrain rotation recrystallization as the dominant recrystallization mechanisms (Figs. 8a-b; e.g. Urai et al., 1986; Bestmann and Prior, 2003). Additionally, high peaks at 5-20º corroborate the presence of subgrains and recrystallized grains (Fig. 13a).

Calcite within the coarse-grained domain from the steep limb (sample PSC 105) shows evidence of abundant twinning, occasionally producing recrystallized grains on the twin planes (Fig. 8c), which is commonly associated with twin boundary migration recrystallization (e.g. Kennedy and White, 2001; Burkhard, 1993). The c-axis maximum oriented ~40˚ clockwise from Z (Fig. 10a) has been observed in other naturally deformed calcite-rich rocks (e.g. Dietrich and Song, 1984; Schmid et al., 1981) and may depend, in part, on the original orientation of grains in the sample. However, such a texture pattern with the development of a monoclinic texture symmetry (Figs. 3b, 10a) is very similar to the texture observed in the twinning regime of Schmid et al. (1987). Calcite twinning rapidly reorients the c-axis into a direction close to the position of the $\sigma 1$ stress axis, and clustering of c-axis maxima is expected

445 to provide good approximation of the direction of maximum tectonic stress during the
446 late stages of deformation (Schmid et al., 1987). Hence, given the pervasive twinning
447 observed in this sample, the oblique concentration of c-axes for PSC 105 (Figs. 3b,
448 10a) is likely due to twinning-related texture, and is consistent with the top-to-the-W
449 sense of shear during dominated simple shear deformation. Clustering of e-poles
450 normal to the foliation – around the Z-axis - (Fig. 10a) and high peaks of neighbor pair
451 grains around 70º in the misorientation graph (Fig. 12a) suggest e-twinning as the
452 main deformation mechanism (e.g. Bestmann et al., 2000).

453 The critical difference in both coarse-grained metacarbonate samples is the
454 orientation of the c-axis maxima at high angles to the grain-shape fabric for PSC 105
455 (at ~40° clockwise from Z) and sub-parallel to the grain-shape fabric for PSC 204 (at
456 ~35° counterclockwise from Z; Fig. 3b). In both cases, the oblique angle between the
457 grain-shape fabric and the foliation is consistent with top-to-the-west shear. Hence,
458 the difference is most likely due to activation of different slip systems and deformation
459 mechanisms. The texture from PSC 105 is consistent with e-twinning, suggestive of
460 σ1 at ~50° counterclockwise to the foliation as expected for top-to-the-west simple
461 shear deformation. However, the texture from sample PSC 204, which lacks pervasive
462 twinning, indicates (c) <a> slip, which is also consistent with simple shear dominated
463 deformation. Both basal <a> (sample PSC 204; Table 1) and e-twinning (sample PSC
464 105) are activated due to intracrystalline plasticity, being the first expected under
465 higher strain conditions (Barnhoorn et al., 2004). Higher strain conditions are expected
466 for sample PSC 204, as it is located in the west quarry, where transposition foliation
467 and long (low-angle) fold limbs occur due to advanced stage of progressive shearing
468 in a simple shear dominant deformation context. Thus, the long limbs of the folds have
469 a more complicated deformation history because of the long-lived rotation during

shearing. This demonstrates the great variety of textures that can be found in naturally deformed marbles, as initially assumed by Wenk et al. (1987), and later demonstrated in several other works (e.g. Kurz et al., 2000; Leiss and Molli, 2002).

Quartz microstructures and textures from samples PSC 105 and PSC 204 indicate activation of dissolution-precipitation mechanism (Table 1), which is also evidenced by the widespread presence of quartz and calcite veins at the outcrops (Fig. 4c; e.g. Groshong, 1988). The boundaries between quartz grains are not straight, but rather undulating with many embayments (white arrows in Fig. 8). The textures, however, are quite different. As quartz c-axes from sample PSC 105 are parallel to the X-axis (Fig. 10a), poles to c-planes from sample PSC 204 are randomly distributed (Fig. 11a). It is widely agreed that dissolution-precipitation creep may help to randomize CPO texture in deformed rocks (e.g. Menegon et al. 2008), which supports the CPO found in sample PSC 204.

Yet, one might suggest that the texture found in quartz from sample PSC 105 is due to activation of prism <c> slip (e.g. Bouchez et al., 1984; Garbutt and Teyssier, 1991) deformed by dislocation creep. However, slip along prism <c> for quartz was reported only in high temperature conditions (e.g. Behr, 1980; Bouchez et al., 1984; Lister and Dornsiepen, 1982; Cavalcante et al., 2018). On the other hand, X-maximum c-axis texture development has also been observed in natural quartz tectonites deformed by dissolution-precipitation creep (e.g. Hippertt, 1994; Takeshita and Hara, 1998; Lagoeiro et al., 2003). Since our rocks are likely deformed under lower greenschist facies (e.g. Magalhães, 1989), activation of temperature sensitive prism <c> is unlikely. Thus, a possible explanation for the c-axis maximum parallel to the X-direction (Figs. 3b, 10a) is controlled-dissolution precipitation mechanism (Table 1). Furthermore, the presence of phyllosilicates might enhance the fluid influx, thus

favoring solution-transfer creep (e.g. Etheridge and Wilkie, 1979; Kerrich, 1978). Minor undulose extinction and subgrains may reflect the slight peak at small angles in the misorientation angle distribution histogram (Fig. 12a), indicating that dynamic recrystallization mechanisms were also deployed during deformation, yet with little contribution to the bulk strain. Additionally, crystal-plastic deformation and solution-precipitation creep mechanisms can be intimately associated or even coexisting processes in tectonites deformed under low- to medium-grade metamorphic conditions (e.g., Hippertt, 1994; Lagoeiro et al., 2003).

7.3 Deformation mechanisms in fine-grained metacarbonates

The fine equigranular fabrics of both quartz and calcite from samples PSC 105 and PSC 204 are similar. Quartz and calcite from both of the long and short limb of the folds displays weak texture strength. However, calcite from sample PSC 204 have the c-axis rotated at ~35° counterclockwise from Z, parallel to the grain shape orientation (Figs. 3b, 11b), as occurs in calcite from the coarse-grained domain. In contrast, calcite c-axis from sample PSC 105 is randomly distributed (Figs. 3b, 10b). Fine-grained domains of both samples lack twinned grains, as shown in the misorientation angle histogram in which e-twinning peak is closely related to the random theoretical curve (Figs. 12b, 13b). Furthermore, the poles to the e-planes are more randomly distributed compared to calcite in the coarse-grained domain (Figs. 10-11). The random (sample PSC 105) and more defined texture (sample PSC 204) observed in the fine-grained calcite can be in part attributed to distinct ways to accommodate the deformation in the long and short limbs of the shear folds.

The mechanism leading to fabric weakening at the sample scale is likely related to the grain size of the minerals. Smaller grain sizes are prone to accommodate the deformation by diffusive mechanisms in dry (diffusion creep) or wet (dissolution creep)

conditions, which usually lead to a weakening of the texture (e.g. Mukai et al., 2014). Veins in the carbonate rocks are common in the outcrops. Therefore, it is likely that fluid-assisted grain boundary sliding played an important role on accommodating the deformation as well as in randomizing the texture for calcite and quartz in sample PSC 105, and for quartz in sample PSC 204. Although calcite most likely controlled the rheology of the rock during deformation, minerals with contrasting behavior may affect the way the deformation is accommodated, as well as the development of textures, which also depends on the proportion of the phases involved. This could also be an important factor in reducing the texture in metacarbonate rocks (PSC105) with a certain proportion of quartz and phyllosilicate grains (e.g. Mehl and Hirth, 2008).

On the other hand, the c-axis texture observed in fine-grained calcite from sample PSC 204 (Fig. 3b) cannot be explained by grain boundary sliding, as this mechanism usually leads to weakening of the texture (Mehl and Hirth, 2008). The orientation of the c-axes parallel to the grain shape fabrics consistent with the top-to-the-west shear sense (Figs. 3b, 11b) suggests that oriented dissolution-precipitation mechanism may also have played a role in accommodating strain in these domains, as evidence for dislocation creep are scarce. Therefore, solution transfer would generate a more oriented microfabric by crystallographic controlled growth, under higher strain conditions expected in the long limbs of the shear folds. Hence, we propose that the crystallographic fabrics found in the fine-grained domains result from a combination of mechanisms that first produced the crystallographic orientation (oriented dissolution-precipitation creep), and those that weaken the texture or even randomize it (fluid-assisted grain boundary sliding), spreading the poles all over the pole figure diagrams (Fig. 3b; Table 1).

8 Conclusion

The accommodation of low temperature thrusting deformation in the foreland of the Araçuaí belt is heterogenous, primarily due to the rheological contrast between quartzites of the Espinhaço Supergroup and metacarbonates of the Bambuí Group. At the microscale, such rheological contrast and heterogeneous distribution of deformation are recorded by a predominance of a single deformation mechanism in the quartzite and by the activation of several deformation mechanisms in the metacarbonate rocks (Table 1), controlled by domains with different grain sizes and compositions, and by strain conditions related to the fold geometry. It demonstrates the large variety of texture-types that may occur in naturally deformed calcite, as pointed out in several works.

The lack of intracrystalline plasticity and random texture of quartz in the quartzite of the Espinhaço Supergroup indicate dissolution-precipitation creep as the major deformation mechanism. Coarse-grained calcite from the short and long limb of the shear-related fold deforms by mechanical twinning and dislocation creep with activation of (c)<a> slip system, respectively, due to intracrystalline plasticity. Twin boundary migration and subgrain rotation recrystallization are widespread. Coarse-grained quartz deforms by dissolution precipitation creep. The fine-grained domains indicate that calcite and quartz in both the long and short limb of the shear-related fold activated fluid-assisted grain boundary sliding.

The top-to-the-W structures observed in quartzite outcrops is consistently reflected in the carbonate rocks (i.e., asymmetric shear folds, pattern of c-axis in coarse-grained calcite). Given the rapid recrystallization of carbonates during shearing, this is considered to be evidence that the last plastic deformation in this

region was related to thrusting, and that the carbonates acted as a weak unit on which allochthonous units could be transported onto the São Francisco Craton.

Acknowledgements

The manuscript has been improved by the reviews of Dr. Simone Papa, Dr. Rüdiger Kilian and two anonymous reviewers. Special thanks are due to Paulo Roberto Roscoe Papini and Maria Cristina Lamego Papini for their hospitality during our stay at Serra do Cipó, and Lucinha for preparing nice meals for the field lunch. Flavia Afonso is acknowledged for helping to prepare marvelous thin sections. Haakon Fossen and Carlos Alberto Rosière are thanked for fruitful discussions and critical comments on the manuscript. We appreciate the Channel Software personnel for technical support throughout the EBSD data processing. This study was financed in part by the Coordenação de Aperfeiçoamento de Pessoal de Nível Superior - Brasil [CAPES] - Finance Code 001 and the Conselho Nacional de Desenvolvimento Científico e Tecnológico [CNPq grant numbers 425412/2018-0 and 305232/2018-5].

9 References

Alkmim, F.F., Kuchenbecker, M., Reis, H.L.S., Pedrosa-Soares, A.C., 2017. The Araçuaí Belt. Springer, Cham, pp. 255–276. https://doi.org/10.1007/978-3-319-01715-0_14

Alkmim, F.F., Marshak, S., Pedrosa-Soares, A.C., Peres, G.G., Cruz, S.C.P., Whittington, A., 2006. Kinematic evolution of the Araçuaí-West Congo orogen in Brazil and Africa: Nutcracker tectonics during the Neoproterozoic assembly of Gondwana. Precambrian Res. 149, 43–64. https://doi.org/10.1016/j.precamres.2006.06.007

Almeida Abreu, P.A., Fernandes, P.C.O., Knauer, L.G., Hartimann, M.B., Donato, M.T.R., Schorcher, H.D., 1986. Elementos da zona de cisalhamento dúctil da borda oriental da Serra do Espinhaço, Minas Gerais. Proceedings of the 34th Congresso Brasileiro de Geologia 3, 1219 - 1231.

Almeida, F.F.M., Litwinski, N., 1984. Província Mantiqueira: Setor setentrional, in O Precambiano do Brasil, 282-307, Edgard Bliicher.

Bacellar, L. de A.P., 1989. Geologia estrutural do Supergrupo São Francisco ao longo da seção regional Coromandel - Três Marias • Conselheiro Mata, MG. Universidade Federal de Ouro Preto.

Barber, D.J., Wenk, H.R., Gomez-Barreiro, J., Rybacki, E., Dresen, G., 2007. Basal slip and texture development in calcite: new results from torsion experiments. Physics and Chemistry of Minerals 34, 73–84.

Barnhoorn, A., Bystricky, M., Burlini, L., Kunze, K., 2004. The role of recrystallisation on the deformation behaviour of calcite rocks: Large strain torsion experiments on Carrara marble. J. Struct. Geol. 26, 885–903. https://doi.org/10.1016/j.jsg.2003.11.024

Bauer, H., Rogowitz, A., Grasemann, B., Decker, K., 2018. Intracrystalline deformation of calcite in the upper brittle crust. Geology 46, 375–378. doi: https://doi.org/10.1130/G39990.1

Behr, H.J., 1980. Polyphase shear zones in the granulite belts along the margins of the Bohemian Massif. J. Struct. Geol. 2, 249–254. https://doi.org/10.1016/0191-8141(80)90057-7

Behrmann, J., 1985. Crystal plasticity and superplasticity in quartzite; A natural example. Tectonophysics 115, 101–129. https://doi.org/10.1016/0040-1951(85)90102-7

Bestmann, M., Kunze, K., Matthews, A., 2000. Evolution of a calcite marble shear zone complex on Thassos Island, Greece: Microstructural and textural fabrics and their kinematic significance. J. Struct. Geol. 22, 1789–1807. https://doi.org/10.1016/S0191-8141(00)00112-7

Bestmann, M., Prior, D.J., 2003. Intragranular dynamic recrystallization in naturally deformed calcite marble: Diffusion accommodated grain boundary sliding as a result of subgrain rotation recrystallization. J. Struct. Geol. 25, 1597–1613. https://doi.org/10.1016/S0191-8141(03)00006-3

Bestmann, M., Prior, D.J., Veltkamp, K.T.., 2004. Development of single-crystal σ-

shaped quartz porphyroclasts by dissolution–precipitation creep in a calcite marble shear zone. J. Struct. Geol. 26, 869–883. https://doi.org/10.1016/J.JSG.2003.10.003

Bouchez, J.L., Mainprice, D.H., Trepied, L. and Doukhan, J.C., 1984. Secondary lineation in a high-T quartzite (Galicia, Spain): an explanation for an abnormal fabric. J. Struct. Geol. 6, 159-165.

Bunge, H.-J., Hans J., 1982. Texture analysis in materials science : mathematical methods. Butterworths, London.

Burkhard, M., 1993. Calcite twins, their geometry, appearance and significance as stress-strain markers and indicators of tectonic regime: a review. J. Struct. Geol. 15, 351–368. https://doi.org/10.1016/0191-8141(93)90132-T

Busch, J.P., Van der Pluijm, B.A., 1995. Calcite textures, microstructures and rheological properties of marble mylonites in the Bancroft shear zone, Ontario, Canada. Journal of Structural Geology 17, 677-688.

Cavalcante, C., Fossen, H., de Almeida, R.P., Hollanda, M.H.B.M., Egydio-Silva, M., 2019. Reviewing the puzzling intracontinental termination of the Araçuaí-West Congo orogenic belt and its implications for orogenic development. Precambrian Res. 322, 85–98. https://doi.org/10.1016/J.PRECAMRES.2018.12.025

Cavalcante, C., Lagoeiro, L., Fossen, H., Egydio-Silva, M., Morales, L.F.G., Ferreira, F., Conte, T., 2018. Temperature constraints on microfabric patterns in quartzofeldsphatic mylonites, Ribeira belt (SE Brazil). Journal of Structural Geology, 115, 243-262. https://doi.org/10.1016/j.jsg.2018.07.013

Chemale Jr., F., Dussin, I.A., Alkmim, F.F., Martins, M.S., Queiroga, G., Armstrong, R., Santos, M.N., 2012. Unravelling a Proterozoic basin history through detrital zircon geochronology: The case of the Espinhaço Supergroup, Minas Gerais, Brazil. Gondwana Res. 22, 200–206. https://doi.org/10.1016/J.GR.2011.08.016

Davis, G.H., Reynolds, S.J., Kluth, C.F., 2011. Structural Geology of Rocks and Regions, 3rd Edition.

De Bresser, J.H.P., Spiers, C.J., 1997. Strength characteristics of the r, f , and c slip systems in calcite. Tectonophysics 1–23.

Dietrich, D., Song, H., 1984. Calcite fabrics in a natural shear environment, the Helvetic nappes of western Switzerland. J. Struct. Geol. 6, 19–32. https://doi.org/10.1016/0191-8141(84)90080-4

Ebert, A., Herwegh, M., Berger, A., Pfifner, A. 2008. Grain coarsening maps for polymineralic carbonate mylonites: A calibration based on data from different Helvetic nappes (Switzerland). Tectonophysics, 457, 128-142.

Etheridge, M.A., Wilkie, J.C., 1979. Grainsize reduction, grain boundary sliding and the flow strength of mylonites. Tectonophysics 58, 159–178. https://doi.org/10.1016/0040-1951(79)90327-5

Faghih, A., Soleimani, M., 2015. Quartz c-axis fabric development associated with shear deformation along an extensional detachment shear zone: Chapedony Metamorphic Core Complex, Central-East Iranian Microcontinent. Journal of Structural Geology, Volume 70, 1-11. https://doi.org/10.1016/j.jsg.2014.10.016.

Garbutt, J.M., Teyssier, C., 1991. Prism 〈c〉 slip in the quartzites of the Oakhurst

Mylonite Belt, California. J. Struct. Geol. 13, 657–666. https://doi.org/10.1016/0191-8141(91)90028-H

Gratier, J.-P., Dysthe, D.K., Renard, F., 2013. The Role of Pressure Solution Creep in the Ductility of the Earth's Upper Crust. Adv. Geophys. 54, 47–179. https://doi.org/10.1016/B978-0-12-380940-7.00002-0

Gray, D.R., 1978. Cleavages in deformed psammitic rocks from southeastern Australia: Their nature and origin. Geol. Soc. Am. Bull. 89, 577. https://doi.org/10.1130/0016-7606(1978)89<577:CIDPRF>2.0.CO;2

Groshong, R.H., 1988. Low Temperature Deformation Mechanisms and their Interpretation. Geol. Soc. Am. Bull. 100, 1329–1360. https://doi.org/10.1130/0016-7606(1988)100<1329:ltdmat>2.3.co;2

Guadagnin, F., Chemale Jr., F., 2015. Detrital zircon record of the Paleoproterozoic to Mesoproterozoic cratonic basins in the São Francisco Craton. J. South Am. Earth Sci. 60, 104–116. https://doi.org/10.1016/J.JSAMES.2015.02.007

Hartmann, M.B., 1987. A Cordilheira do Espinhaço meridional (Minas Gerais), Registro de uma tectônica de colisão continental no final do Proterozoico. Preceedings of the 1st Simpósio Nacional de Estudos Tectônicos, 71-73, Salvador, Brazil.

Herrgesell, G., Pflug, R., 1986. The Thrust Belt of the Southern Serra do Espinhaço, Minas Gerais, Brazil. Zentralblatt für Geol. und Paläontologie, Tl. I 1985, 1405–1414. https://doi.org/10.1127/zbl_geol_pal_1/1985/1986/1405

Hippertt, J.F., 1994. Microstructures and c-axis fabrics indicative of quartz dissolution in sheared quartzites and phyllonites. Tectonophysics 229, 141–163. https://doi.org/10.1016/0040-1951(94)90026-4

Kennedy, L.A., White, J.C., 2001. Low-temperature recrystallization in calcite: Mechanisms and consequences. Geology 29, 1027–1030. doi: https://doi.org/10.1130/0091-7613(2001)029<1027:LTRICM>2.0.CO;2

Kerrich, R., 1978. An historical review and synthesis of research on pressure solution. Zentralblatt für Geol. und Paläontologie 1, 512–550.

Kilian, R., Heilbronner, R., 2017. Analysis of crystallographic preferred orientations of experimentally deformed Black Hills Quartzite. Solid Earth 8, 1095–1117. https://doi.org/10.5194/se-8-1095-2017

Kurz, W., Neubauer, F., Unzog, W., Genser, J., Wang, X., 2000. Microstructural and textural development of calcite marbles during polyphase deformation of Penninic units within the Tauern Window (Eastern Alps). Tectonophysics 316, 327–342.

Lagoeiro, L., Hippertt, J., Lana, C., 2003. Deformation partitioning during folding and transposition of quartz layers. Tectonophysics 361, 171–186. https://doi.org/10.1016/S0040-1951(02)00585-1

Leiss, M., Molli,. 2002. 'High temperature' texture in naturally deformed Carrara marble from the Alpi Apuane, Italy. Journal of Structural Geology 25, 649-658.

Lister, G.., Dornsiepen, U.., 1982. Fabric transitions in the Saxony granulite terrain. J. Struct. Geol. 4, 81–92. https://doi.org/10.1016/0191-8141(82)90009-8

Lister, G.S., Paterson, M.S., Hobbs, B.E., 1978. The simulation of fabric development in plastic deformation and its application to quartzite: The model. Tectonophysics 45, 107–158. https://doi.org/10.1016/0040-1951(78)90004-5

Lloyd, G.E., 2004. Microstructural evolution in a mylonitic quartz simple shear zone: the significant roles of dauphine twinning and misorientation. Geol. Soc. London, Spec. Publ. 224, 39–61. https://doi.org/10.1144/GSL.SP.2004.224.01.04

Magalhães, P.M., 1989. Análise estrutural qualitativa das rochas do Grupo Bambuí na porção sudoeste da Bacia do São Francisco. Universidade Federal de Ouro Preto.

Marshak, S., Alkmim, F.F., 1989. Proterozoic contraction/extension tectonics of the southern SÃO Francisco Region, Minas Gerais, Brazil. Tectonics 8, 555–571. https://doi.org/10.1029/TC008i003p00555

Marshak, S., Alkmim, F.F., Whittington, A., Pedrosa-Soares, A.C., 2006. Extensional collapse in the Neoproterozoic Araçuaí orogen, eastern Brazil: a setting for reactivation of asymmetric crenulation cleavage. J. Struct. Geol. 28, 129–147. https://doi.org/10.1016/J.JSG.2005.09.006

Martins-Neto, M.., Pedrosa-Soares, A.., Lima, S.A.., 2001. Tectono-sedimentary evolution of sedimentary basins from Late Paleoproterozoic to Late Neoproterozoic in the São Francisco craton and Araçuaí fold belt, eastern Brazil. Sediment. Geol. 141–142, 343–370. https://doi.org/10.1016/S0037-0738(01)00082-3

McPherren, E.D., Kuiper, Y.D., 2013. The effects of Dissolution–Precipitation Creep on quartz fabrics within the Purgatory Conglomerate, Rhode Island. J. Struct. Geol. 51, 105–117. https://doi.org/10.1016/J.JSG.2013.03.002

Mehl, L., Hirth, G., 2008. Plagioclase preferred orientation in layered mylonites: Evaluation of flow laws for the lower crust. J. Geophys. Res. Solid Earth 113. https://doi.org/10.1029/2007JB005075

Menegon, L., Pennacchioni, G., Spiess, R., 2008. Dissolution-precipitation creep of K-feldspar in mid-crustal granite mylonites. J. Struct. Geol. 30, 565–579. https://doi.org/10.1016/j.jsg.2008.02.001

Menegon, L., Piazolo, S., Pennacchioni, G., 2011. The effect of Dauphiné twinning on plastic strain in quartz. Contrib. to Mineral. Petrol. 161, 635–652. https://doi.org/10.1007/s00410-010-0554-7

Molli, G., Cortecci. G., Vaselli, L., Ottria, G., Cortopassi, A., Dinelli, E., Mussi, M., Barbieri, M., 2010. Fault zone structure and fluid–rock interaction of a high angle normal fault in Carrara marble (NW Tuscany, Italy). Journal of Structural Geology, 32, 1334-1348.

Molli, G., White, J.C., Kennedy, L., Taini, V., 2011. Low-temperature deformation of limestone, Isola Palmaria, northern Apennine, Italy—the role of primary textures, pre- cursory veins and intracrystalline deformation in localization. Journal of Structural Geology 33, 255–270.

Moreira, D.S., Uhlein, A., Dussin, I.A., Uhlein, G.J., Pimentel Misuzaki, A.M., 2020. A Cambrian age for the upper Bambuí Group, Brazil, supported by the first U-Pb dating of volcaniclastic bed. J. South Am. Earth Sci. 99, 102503. https://doi.org/10.1016/J.JSAMES.2020.102503

Mukai, H., Austrheim, H., Putnis, C. V., Putnis, A., 2014. Textural evolution of plagioclase feldspar across a shear zone: Implications for deformation mechanism and rock strength. J. Petrol. 55, 1457–1477. https://doi.org/10.1093/petrology/egu030

Padrón-Navarta, J.A., Tommasi, A., Garrido, C.J., López Sánchez-Vizcaíno, V., 2012. Plastic deformation and development of antigorite crystal preferred orientation in high-pressure serpentinites. Earth Planet. Sci. Lett. https://doi.org/10.1016/j.epsl.2012.06.049

Paula-Santos, G.M., Babinski, M., Kuchenbecker, M., Caetano-Filho, S., Trindade, R.I., Pedrosa-Soares, A.C., 2015. New evidence of an Ediacaran age for the Bambuí Group in southern São Francisco craton (eastern Brazil) from zircon U–Pb data and isotope chemostratigraphy. Gondwana Res. 28, 702–720. https://doi.org/10.1016/J.GR.2014.07.012

Pearce, M.A., Wheeler, J., 2011. Grain growth and the lifetime of diffusion creep deformation. Geol. Soc. London, Spec. Publ. 360, 257–272. https://doi.org/10.1144/SP360.15

Pennacchioni, G., Menegon, L., Leiss, B., Nestola, F., Bromiley, G., 2010. Development of crystallographic preferred orientation and microstructure during plastic deformation of natural coarse-grained quartz veins. J. Geophys. Res. Solid Earth 115. https://doi.org/10.1029/2010JB007674

Philpotts, A., Ague, J., 2009. Principles of Igneous and Metamorphic Petrology, Principles of Igneous and Metamorphic Petrology. Cambridge University Press. https://doi.org/10.1017/cbo9780511813429

Pimentel, M.M., Rodrigues, J.B., DellaGiustina, M.E.S., Junges, S., Matteini, M., Armstrong, R., 2011. The tectonic evolution of the Neoproterozoic Brasília Belt, central Brazil, based on SHRIMP and LA-ICPMS U-Pb sedimentary provenance data: A review. J. South Am. Earth Sci. 31, 345–357. https://doi.org/10.1016/j.jsames.2011.02.011

Putnis, A., Austrheim, H., 2010. Fluid-induced processes: Metasomatism and metamorphism. Geofluids 254–269. https://doi.org/10.1111/j.1468-8123.2010.00285.x

Rogowitz, A., White, J.C., Grasemann, B., 2016. Strain localization in ultramylonitic marbles by simultaneous activation of dislocation motion and grain boundary sliding (Syros, Greece). Solid Earth 7. https://doi.org/10.5194/se-7-355-2016

Rutter, E. H. 1995. Experimental study of the influence of stress, temperature, and strain on the dynamic recrystallization of Carrara marble. Journal of Geophysical Research 24,651-663.

Santos, M.N., Chemale, F., Dussin, I.A., Martins, M., Assis, T.A.R., Jelinek, A.R., Guadagnin, F., Armstrong, R., 2013. Sedimentological and paleoenvironmental constraints of the Statherian and Stenian Espinhaço rift system, Brazil. Sediment. Geol. 290, 47–59. https://doi.org/10.1016/J.SEDGEO.2013.03.002

Schmid, S.M., Boland, J.N., Paterson, M.S., 1977. Superplastic flow in finegrained limestone. Tectonophysics 43, 257–291. https://doi.org/10.1016/0040-1951(77)90120-2

Schmid, S.M., Casey, M., Starkey, J., 1981. The microfabric of calcite tectonites

from the Helvetic Nappes (Swiss Alps). Geol. Soc. London, Spec. Publ. 9, 151–158. https://doi.org/10.1144/GSL.SP.1981.009.01.13

Schmid, S.M., Panozzo, R., Bauer, S., 1987. Simple shear experiments on calcite rocks: rheology and microfabric. J. Struct. Geol. 9, 747–778. https://doi.org/10.1016/0191-8141(87)90157-X

Shaocheng, J., David, M., 1988. Natural deformation fabrics of plagioclase: implications for slip systems and seismic anisotropy. Tectonophysics 147, 145–163. https://doi.org/10.1016/0040-1951(88)90153-9

Skemer, P., Katayama, I., Jiang, Z., Karato, S.I., 2005. The misorientation index: development of a new method for calculating the strength of lattice-preferred orientation. Tectonophysics 411, 157-167. http://dx.doi.org/10.1016/j.tecto.2005.08.023.

Stipp, M., Stünitz, H., Heilbronner, R., Schmid, S.M., 2002. The eastern Tonale fault zone: A “natural laboratory” for crystal plastic deformation of quartz over a temperature range from 250 to 700°C. J. Struct. Geol. 24, 1861–1884. https://doi.org/10.1016/S0191-8141(02)00035-4

Süssenberger, A., Neves, B.B. de B., Wemmer, K., Süssenberger, A., Neves, B.B. de B., Wemmer, K., 2014. Dating low-grade metamorphism and deformation of the Espinhaço Supergroup in the Chapada Diamantina (Bahia, NE Brazil): a K/Ar fine-fraction study. Brazilian J. Geol. 44, 207–220. https://doi.org/10.5327/Z2317-4889201400020003

Takeshita, T., Hara, I., 1998. C-Axis Fabrics and Microstructures in a Recrystallized Quartz Vein Deformed Under Fluid-Rich Greenschist Conditions. J. Struct. Geol. 20, 417–431. https://doi.org/10.1016/S0191-8141(97)00108-9

Tommasi, A., Vauchez, A., 2015. Heterogeneity and anisotropy in the lithospheric mantle. Tectonophysics 661, 11-37. https://doi.org/10.1016/j.tecto.2015.07.026.

Tuller, M.P., Ribeiro, J.H., Signorelli, N., Féboli, W.L., Pinho, J.M.M., 2010. Projeto Sete Lagoas - Abaeté, CPRM. Belo Horionte, Brazil.

Tullis, J., 1990. Experimental studies of deformation mechanisms and microstructures in quartzo-feldspathic rocks. In: Deformation Processes in Minerals, Ceramics and Rocks. The Mineralogical Society Series, vol 1. Springer, Dordrecht. https://doi.org/10.1007/978-94-011-6827-4_9

Uhlein, A., 1991. Transição cráton - faixa dobrada : exemplo do Craton do São Franclsco e da Faixa Araçuaí (ciclo brasiliano) no estado de Minas Gerais: aspectos estratigráficos e estruturais. Universidade de São Paulo.

Urai, J.L., Means, W.D., Lister, G.S., 1986. Dynamic recrystallization of minerals. In: Hobbs, B.E., Heard, H.C., (Eds.). Mineral and Rock Deformation: Laboratory Studies (the Paterson Volume). Geophysical Monograph of American Geophysical Union 36, 161–200.

Van der Pluijm, B., 1991. Marble myionites in the Bancroft shear zone, Ontario, Canada: microstructures and deformation mechanisms. J. Struct. Geol. 13, 1125–1135.

Vauchez, A., Clerc, C., Bestani, L., Lagabrielle, Y., Chauvet, A., Lahfid, A., Mainprice, D., 2013. Preorogenic exhumation of the North Pyrenean Agly massif

(Eastern Pyrenees-France). Tectonics 32, 95–106. DOI:10.1002/tect.20015.

Warren, L.V., Quaglio, F., Riccomini, C., Simões, M.G., Poiré, D.G., Strikis, N.M., Anelli, L.E., Strikis, P.C., 2014. The puzzle assembled: Ediacaran guide fossil Cloudina reveals an old proto-Gondwana seaway. Geology 42, 391–394. https://doi.org/10.1130/G35304.1

Wassmann, S., Stöckhert, B., 2013. Low stress deformation of garnet by incongruent dissolution precipitation creep. J. Struct. Geol. 46, 200–219. https://doi.org/10.1016/j.jsg.2012.09.002

Wenk, H.R., Takeshita, T., Bechler, E., Erskine, B.G., Matthies, S., 1987. Pure shear and simple shear on calcite textures. Comparison of experimental, theoretical and natural data. Journal of Structural Geology 9, 731–745.

Wheeler, J., Prior, D., Jiang, Z., Spiess, R., Trimby, P., 2001. The petrological significance of misorientations between grains. Contrib. to Mineral. Petrol. 141, 109–124. https://doi.org/10.1007/s004100000225

Winkler, H.G.F., 1979. Petrogenesis of metamorphic rocks. Springer-Verlag.

Wintsch, R.P., Aleinikoff, J.N., Yi, K., 2005. Foliation development and reaction softening by dissolution and precipitation in the transformation of granodiorite to orthogneiss, Glastonbury Complex, Connecticut, U.S.A. Can. Mineral. 43, 327–347. https://doi.org/10.2113/gscanmin.43.1.327

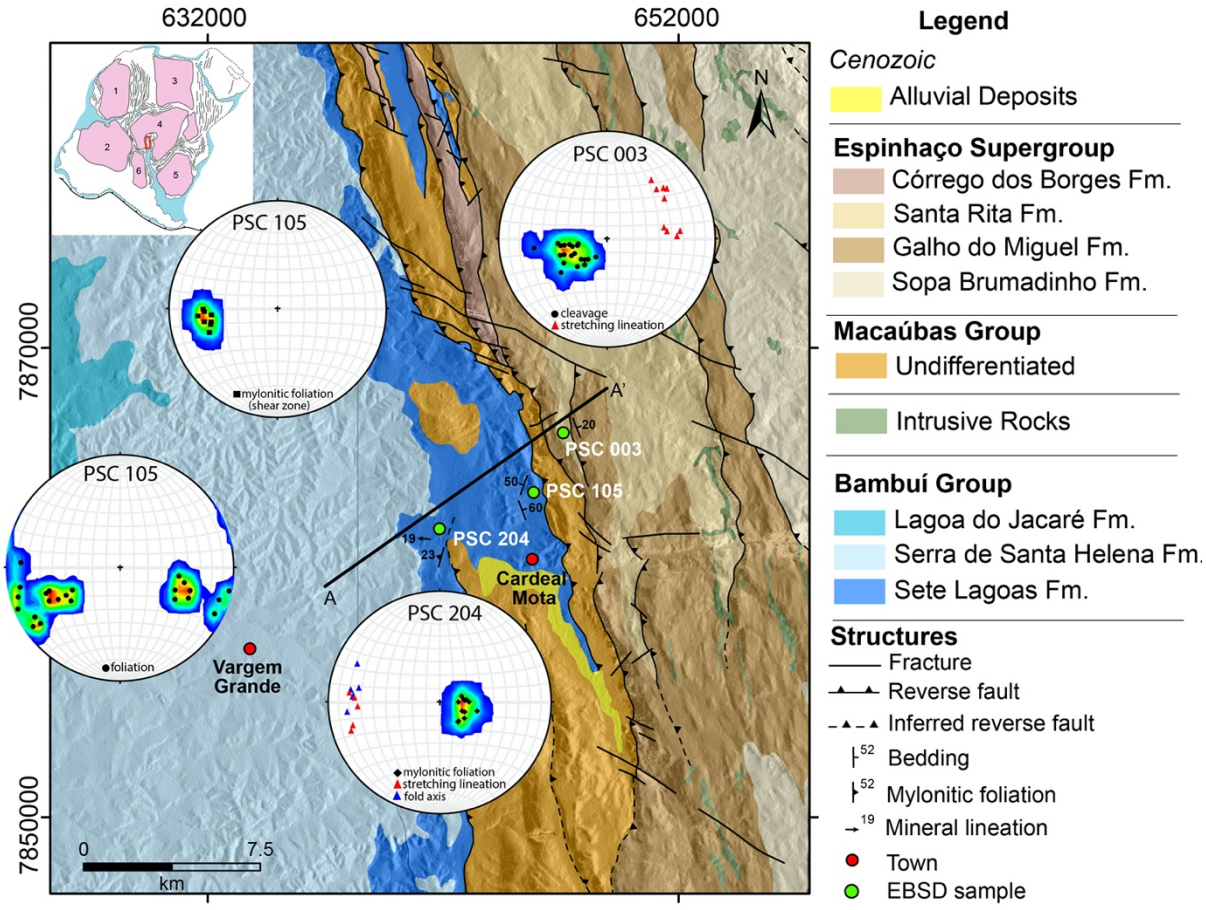

Figure 1: Geological map of the study area superposed onto a digital elevation model. Also shown are stereoplots with structural data for the three study areas. Modified from Oliveira et al. (1997) and from http://geowebapp.cprm.gov.br/ViewerWEB/index_projetos.html). Inset box is a schematic reconstruction of West Gondwana showing the location of the study area (red rectangle) and cratons: 1=West African, 2=Amazonian, 3=Trans Sahara, 4=São Francisco-Congo, 5=Kalahari and 6=Rio de la Plata. See Fig. 2 for cross-section.

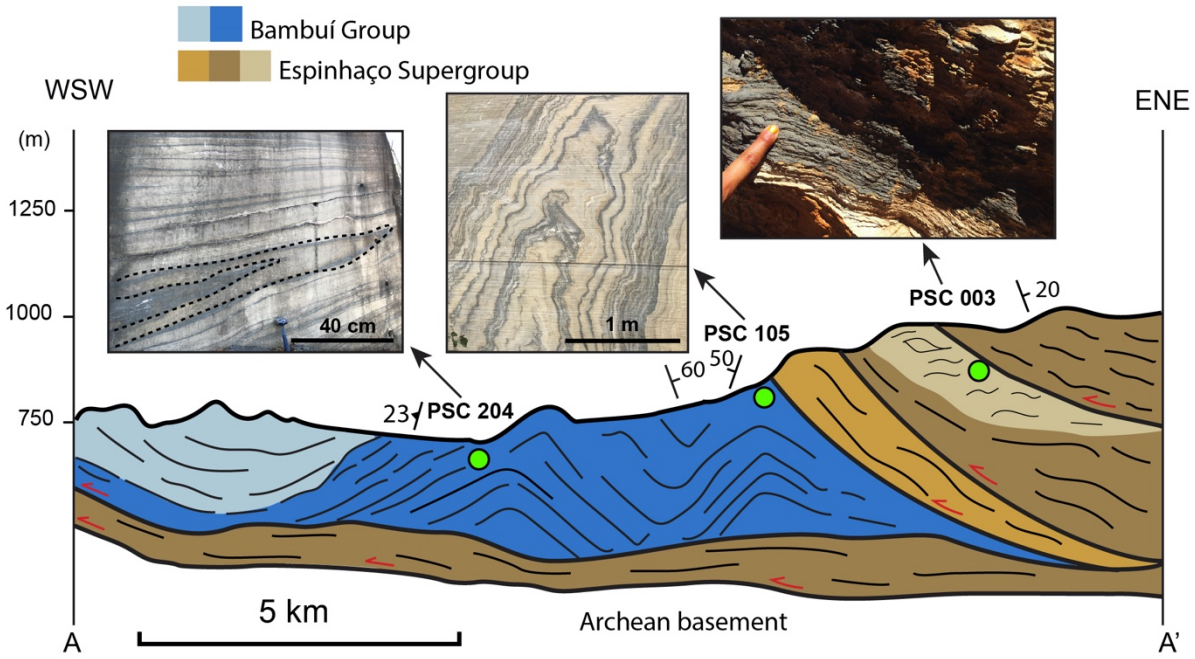

Figure 2: Geological cross-section (profile A-A' as indicated in Fig. 1) through the Espinhaço Supergroup and Bambuí Group, showing the main structural features at each studied outcrop (green dots). Modified from Oliveira et al. (1997); Marshak and Alkmim (1989).

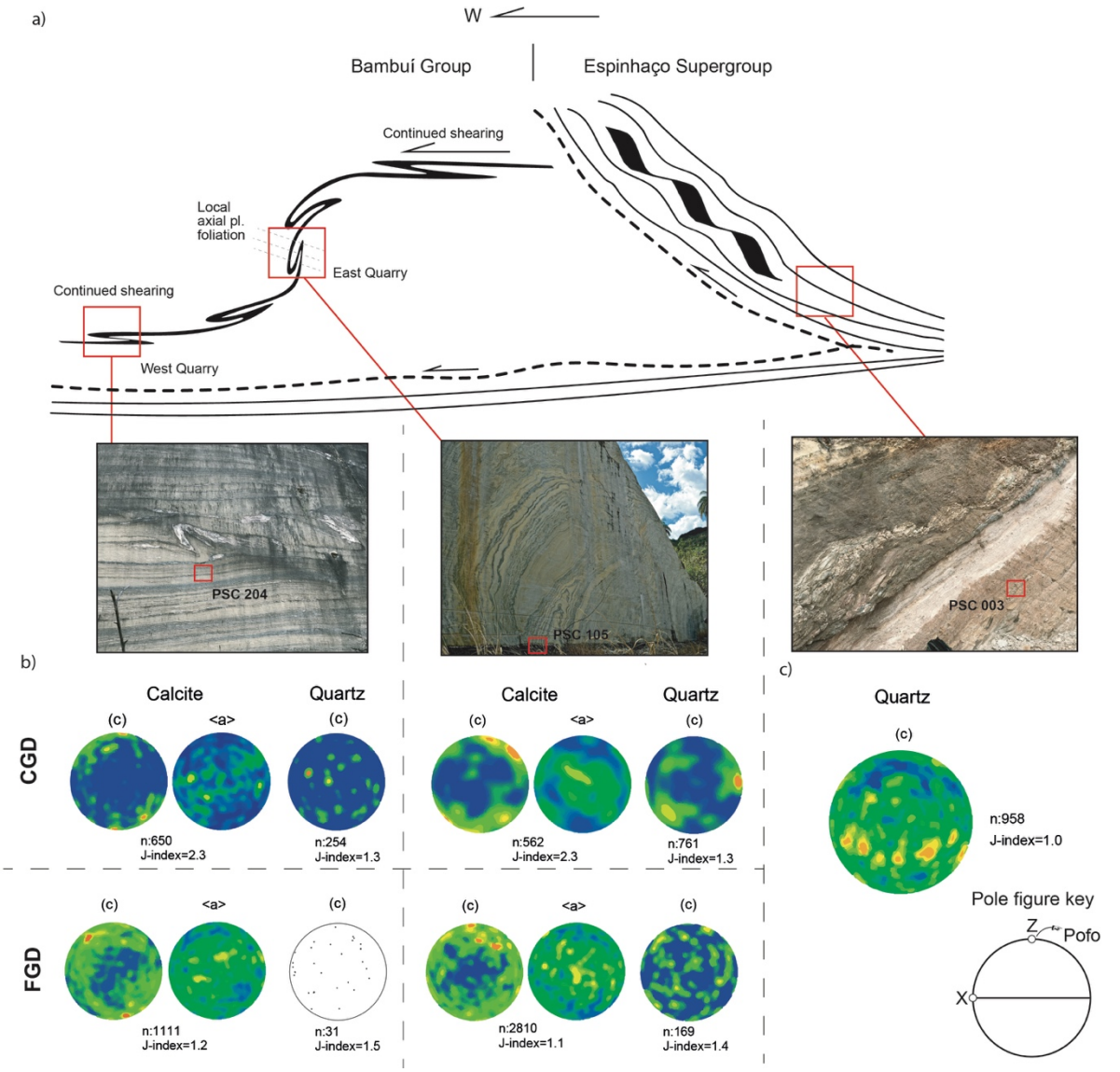

Figure 3: Interpreted structural framework with images for metacarbonates from the Bambuí Group and quartzites from the Espinhaço Supergroup. (a) Sketch illustrating that continued shearing of the metacarbonates produced a large-scale shear-fold, with long (low-angle) limbs (western quarry - sample PSC 204) and short (steep) limbs (eastern quarry – sample PSC 105). (b) Pole figures for quartz c-planes and for calcite c-planes and a-axis from the CGD (coarse-grained domain) and FGD (fine-grained domain) to allow comparison between the different textures and their respective locations, as discussed later. (c) Pole figure for quartz c-planes from the quartzite unit. The foliation is extracted from hand samples and runs vertically east to west. All pole figures are equal area upper hemisphere projections. See Figures 9, 10 and 11 for more details.

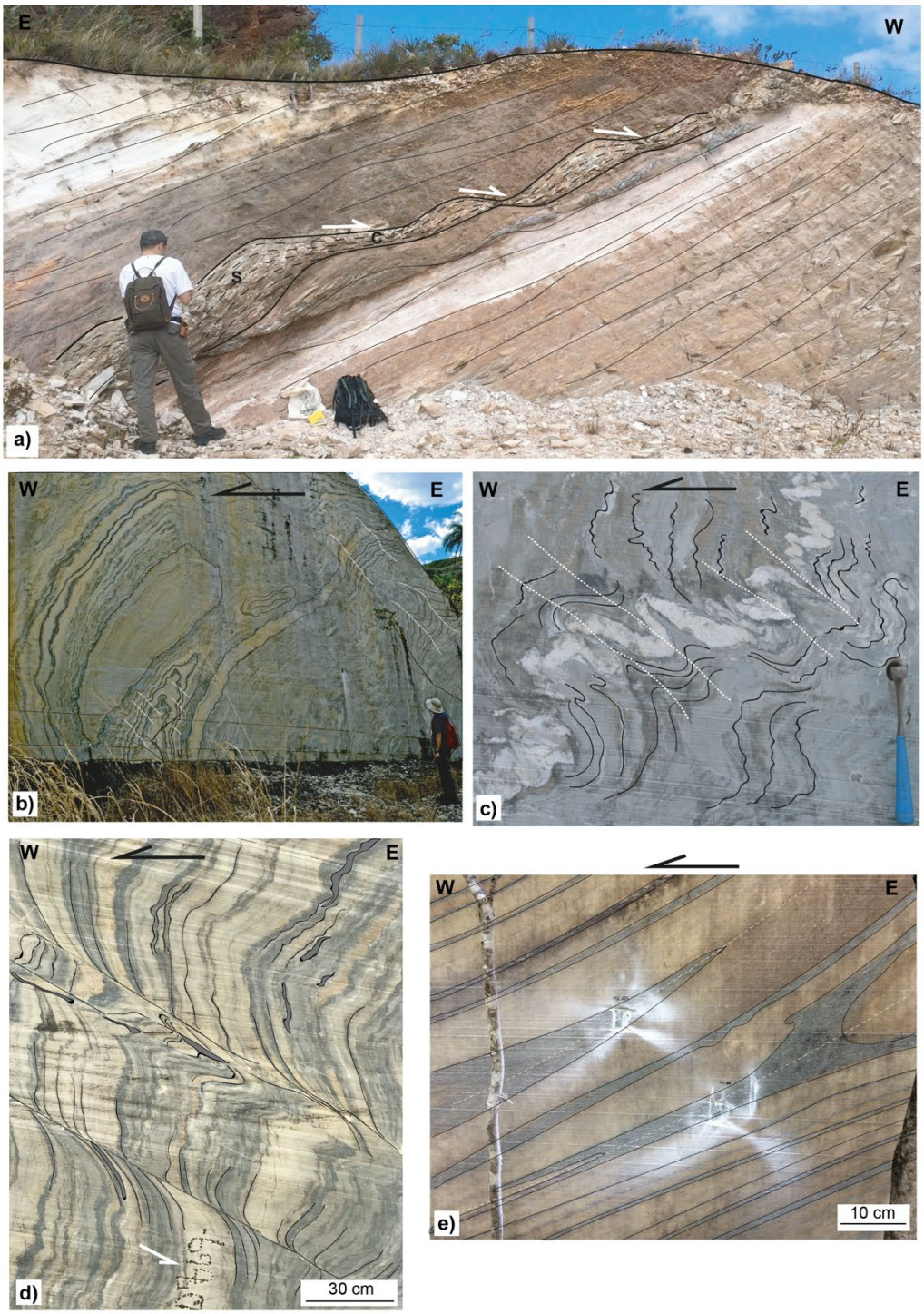

Figure 4: Main structural features of the investigated rocks. Photos (b), (c), and (d): East Quarry at the base of the Espinhaço Range. Photo (e): West Quarry. Dashed line runs parallel to the axial fold planes. (a) Asymmetric boudins in quartz-phyllosilicate-rich vein within the quartzite unit. The S-C fabric developed within the boudins indicates a top to the west shear sense. (b) Sheath and plunging inclined folds in the metacarbonate unit at the East Quarry. (c) Overturned folds in quartz and calcite veins with inclined axial plane. (d) Centimetric shear zones parallel to the folds axial plane. (e) Completely transposed mylonitic foliation in recumbent folded metacarbonates in the West Quarry.

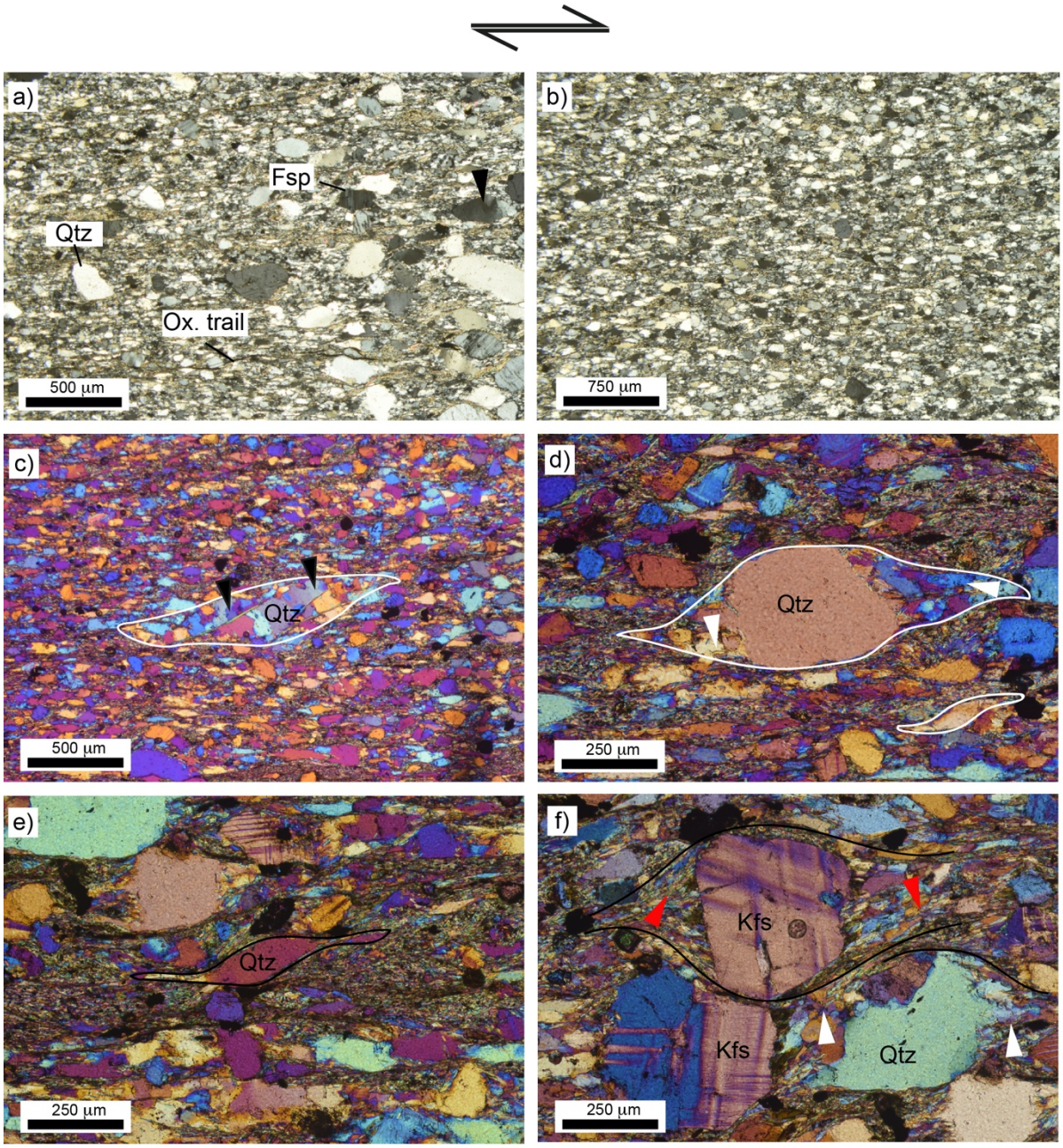

Figure 5: Photomicrographs of representative microstructures in the quartzites. (a) Quartz and feldspar grains in fine-grained matrix with small oxide tails along the cleavage. Phyllosilicates define the cleavage plane that runs horizontally. (b) Matrix with flattened grains parallel to cleavage (MF = foliation). (c) Subgrains and recrystallized quartz grains (black arrows). (d) Quartz sigma-type grain surrounded by pressure shadow with mica beard (white arrows); (e) Quartz fish-shaped microstructure with overgrowth of quartz. (f) Relict feldspar grain with deflected foliation: red arrows show enrichment of mica beard around feldspar in low-pressure shadow zones. Photomicrographs (c), (d), (e) and (f) were taken under crossed polarizers and with a gypsum plate. In all figures, cleavage runs horizontally and the sense of shear is top to the west.

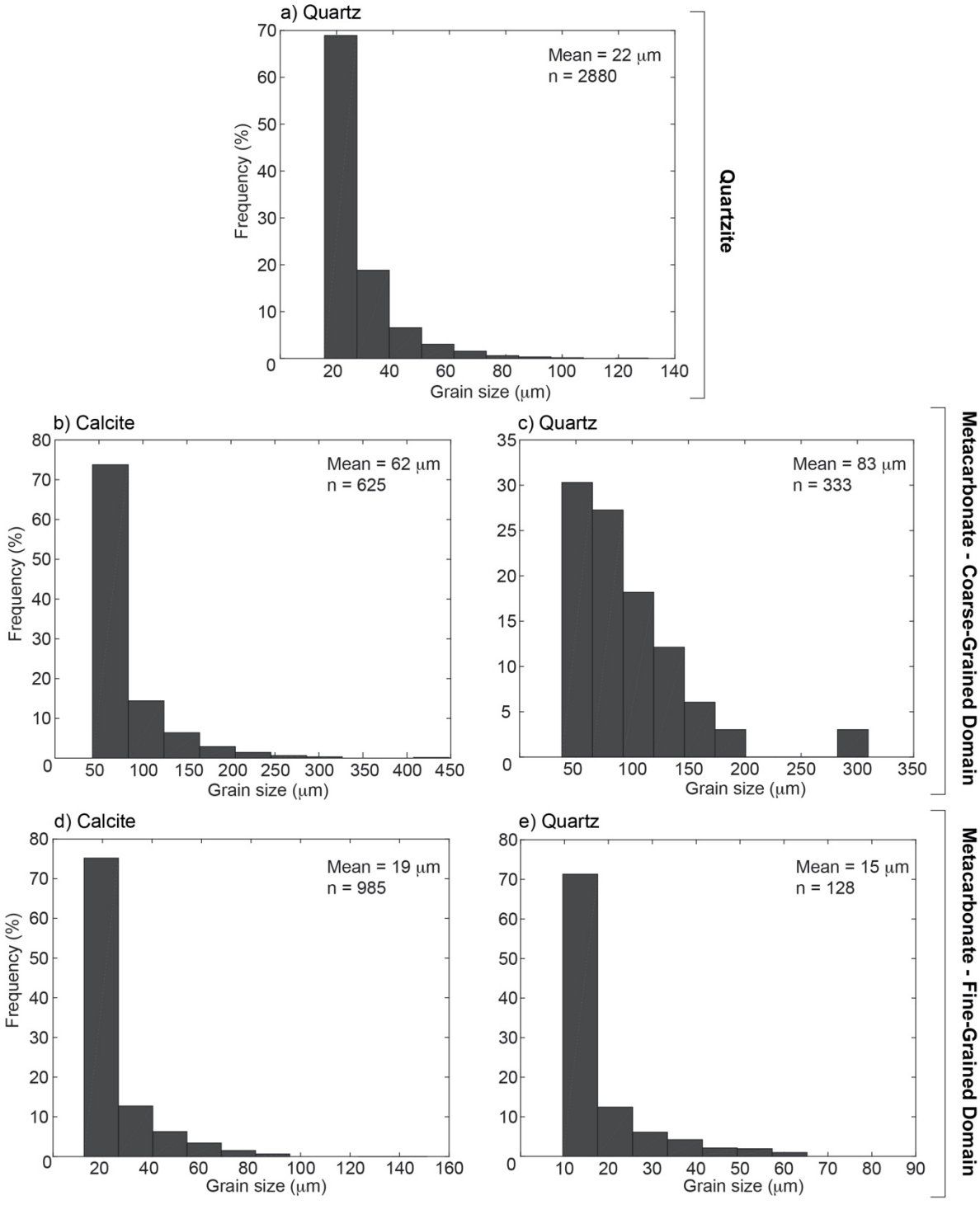

Figure 6: Grain size distributions in the quartzite and metacarbonate rocks. (a) Quartz from the quartzite; (b) calcite and (c) quartz in the coarse-grained domain; (d) calcite and (e) quartz in the fine-grained domain of the metacarbonate.

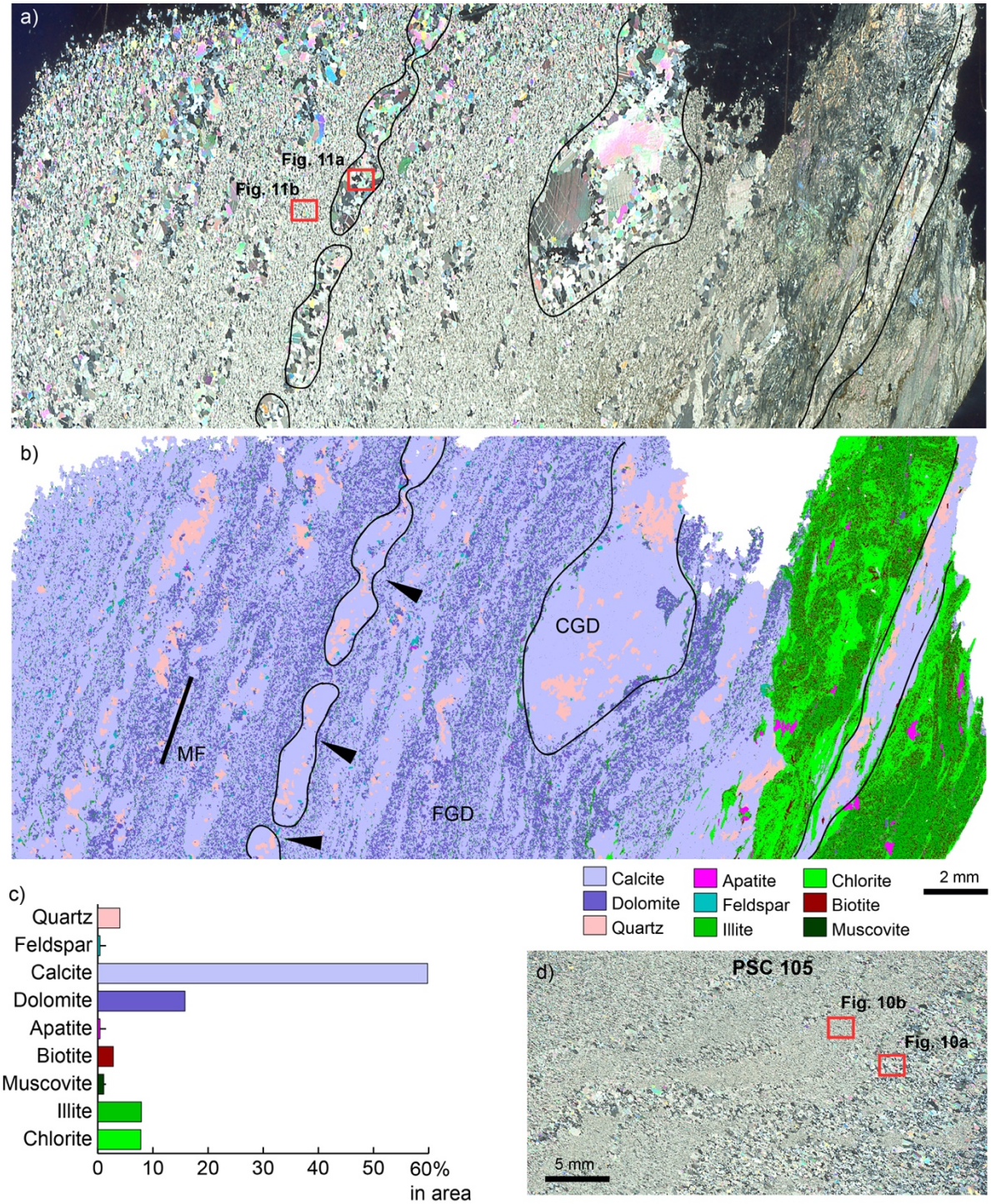

Figure 7: (a) Cross-polarized image and; (b) Modal analysis of sample PSC 204 from the metacarbonate unit located towards the west of the study area. Red boxes indicate areas where EBSD maps were collected. The modal analysis (c) shows that calcite and quartz comprise most of the coarse-grained domain (CGD), while calcite, dolomite, phyllosilicates, apatite, quartz, and feldspar compose the fine-grained domain (FGD). Phyllosilicates are clustered at the upper portion of the thin section. Note some microboudins (black arrows) that consist of coarse calcite and quartz grains. (d) This section scan of sample PSC 105 indicating the areas where EBSD maps were collected (red boxes). MF = foliation.

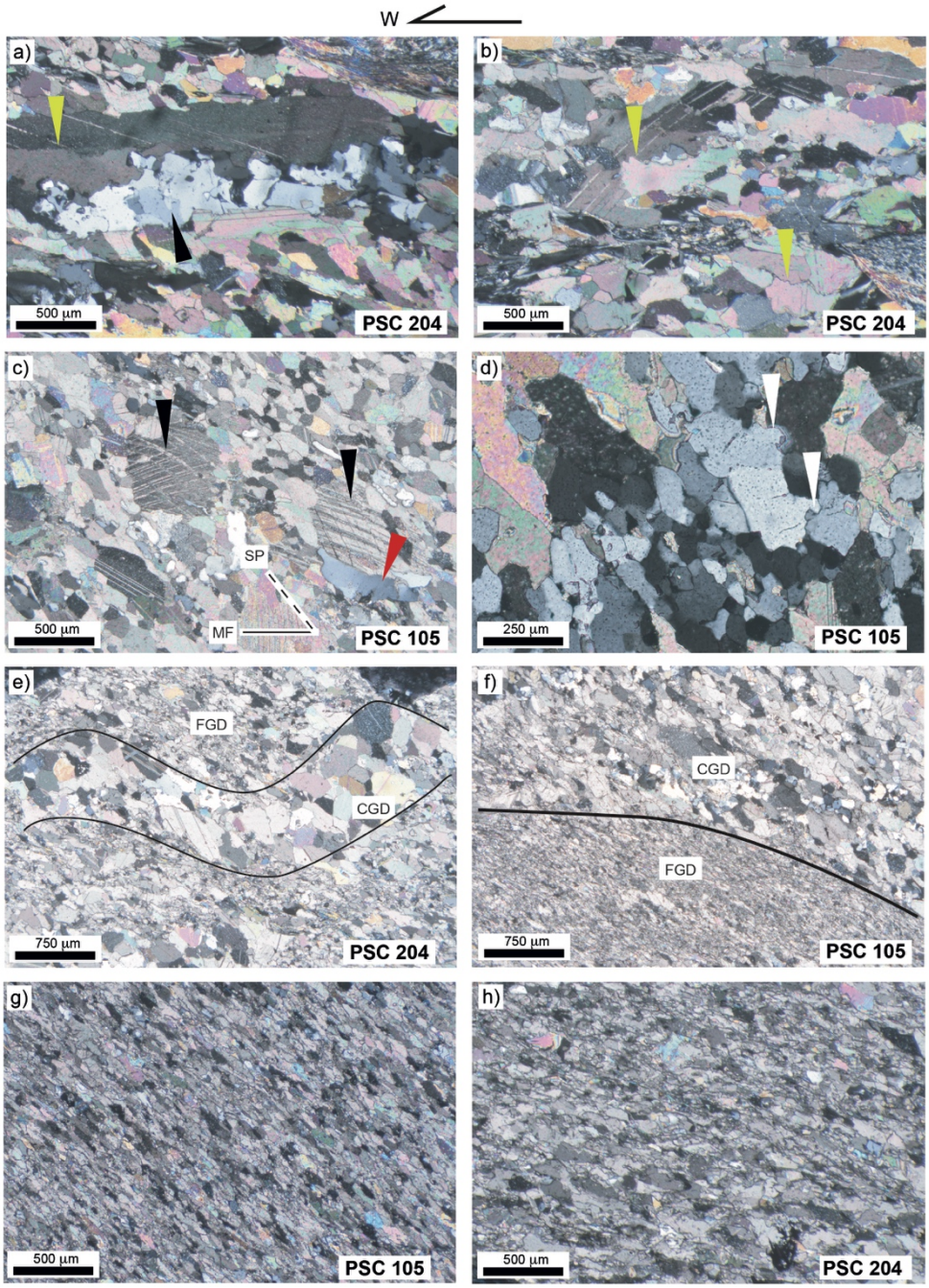

Figure 8: Photomicrographs showing representative microstructures in the metacarbonates. (a) Serrated to straight boundary (yellow arrow) between calcite grains, and bulbous boundary between quartz grains (black arrow) within the CGD. (b) Serrated to curved grain boundary between calcite grains (yellow arrow). (c) Sets of twins in calcite within the CGD. Black arrows show recrystallized calcite on the twin planes. Red arrow indicates undulose extinction and subgrain in quartz. (d) Lobate and bulbous quartz grain contact within the CGD. (e) Folded aggregates of calcite and quartz of the CGD within the FGD. (f) Sharp boundary between CGD and FGD. (g) and (h) Shape preferred orientation of carbonate minerals within the FGD. Microphotographs were taken under crossed polarizes. In all figures, the foliation plane (MF) runs horizontally and shape preferred orientation of grains (SP) is perpendicular to the foliation plane. The foliation plane was extracted from hand samples macroscopic foliation. Sense of shear is top to the west. CGD: coarse-grained domain. FGD: fine-grained domain.

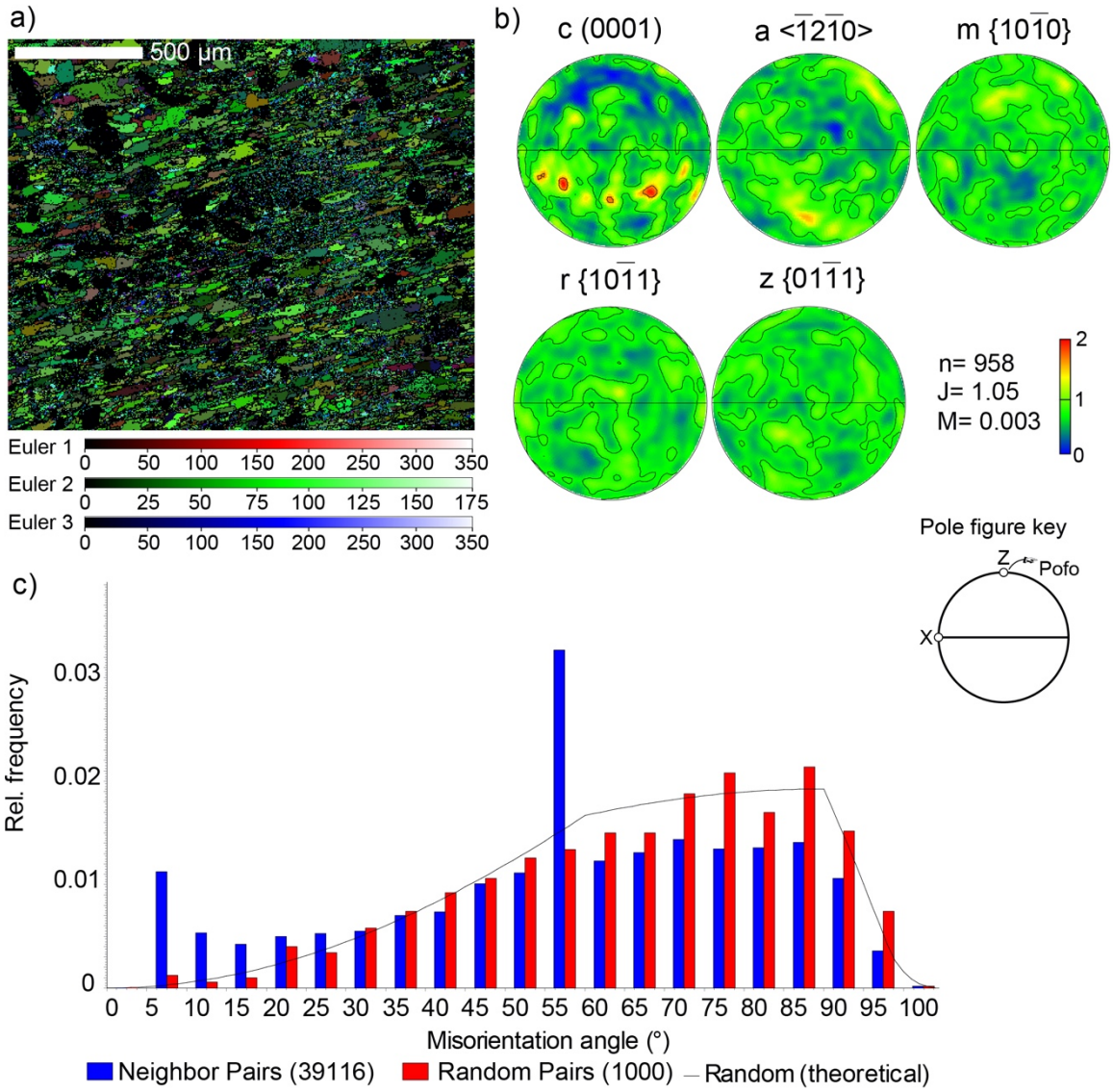

Figure 9: EBSD data from sample PSC003. (a) Orientation map with Euller angles. (b) Pole figures and; (c) Misorientation angle distribution for quartz in the quartzite unit. The pole figures are equal area upper hemisphere projections, with cluster size of 10º. All data represent one point per grain. Z=pole to foliation (Pofo); X=stretching direction. The foliation is extracted from hand samples and runs vertically east to west in the pole figure. N=number of grains. J=J-index. M=M-index.

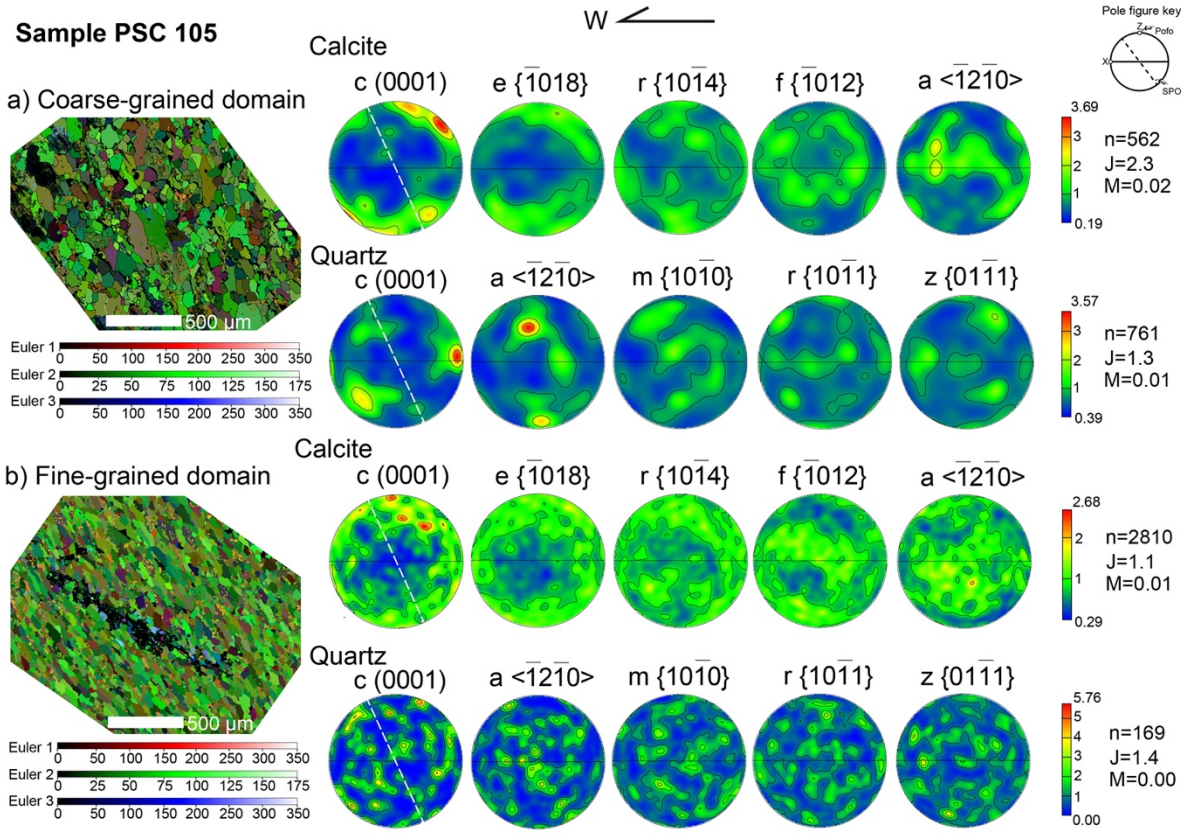

Figure 10: EBSD pole figures for calcite and quartz. (a) Coarse-grained domain and; (b) Fine-grained domain from sample PSC 105. Dashed line represents the shape preferred orientation of the grains in thin section. Z=pole to foliation; X=stretching direction. The foliation is extracted from hand samples and runs vertically east to west. The dashed line represents the shape preferred orientation of the grains (SPO) which makes an angle to the foliation. All pole figures are equal area upper hemisphere projections, with cluster size of 10º. The data represent one point per grain. n: number of grains; J=J-index; Ma=M-index.

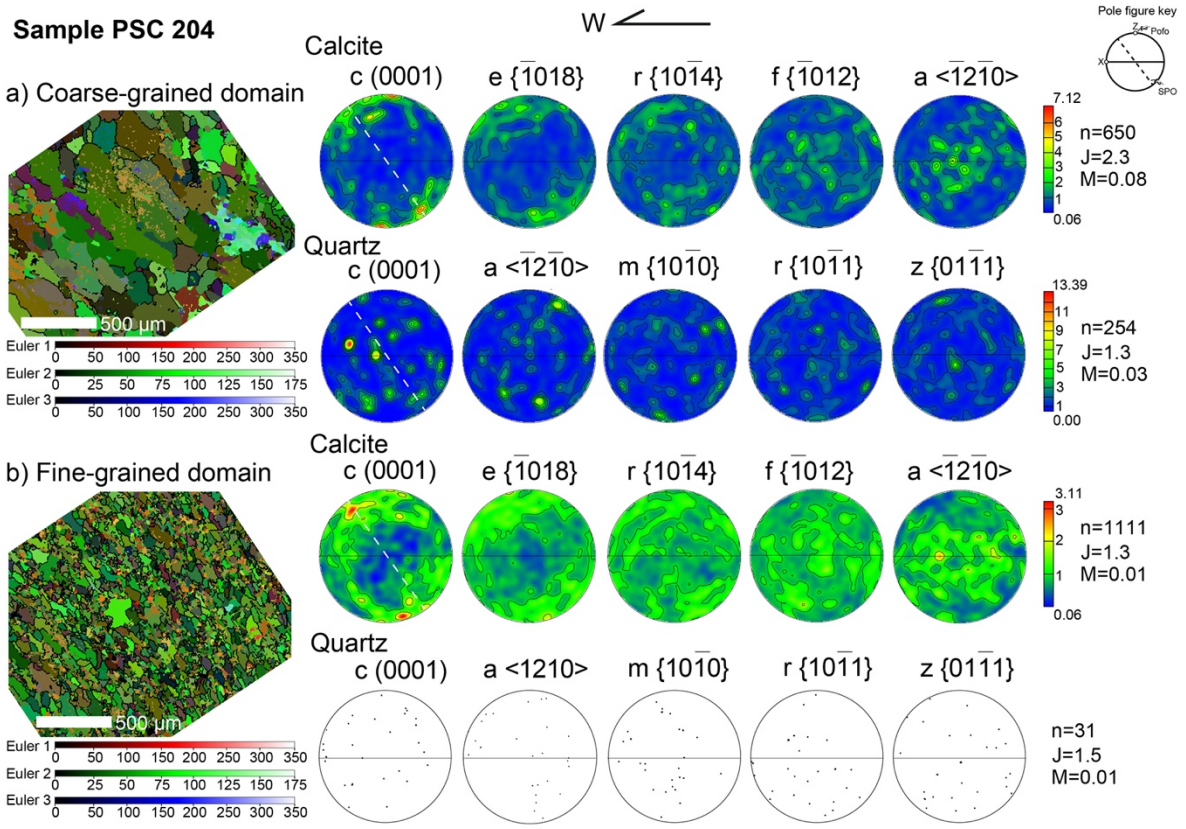

Figure 11: EBSD pole figures for calcite and quartz. (a) Coarse-grained domain and; (b) Fine-grained domain from sample PSC 204. Dashed line represents the shape preferred orientation of the grains in thin section. Z=pole to foliation; X=stretching direction. The foliation is extracted from hand samples and runs vertically east to west. The dashed line represents the shape preferred orientation of the grains (SPO) which makes an angle to the foliation. All pole figures are equal area upper hemisphere projections with cluster size of 10º. The data represent one point per grain. n= number of grains; J=J-index; M=M-index.

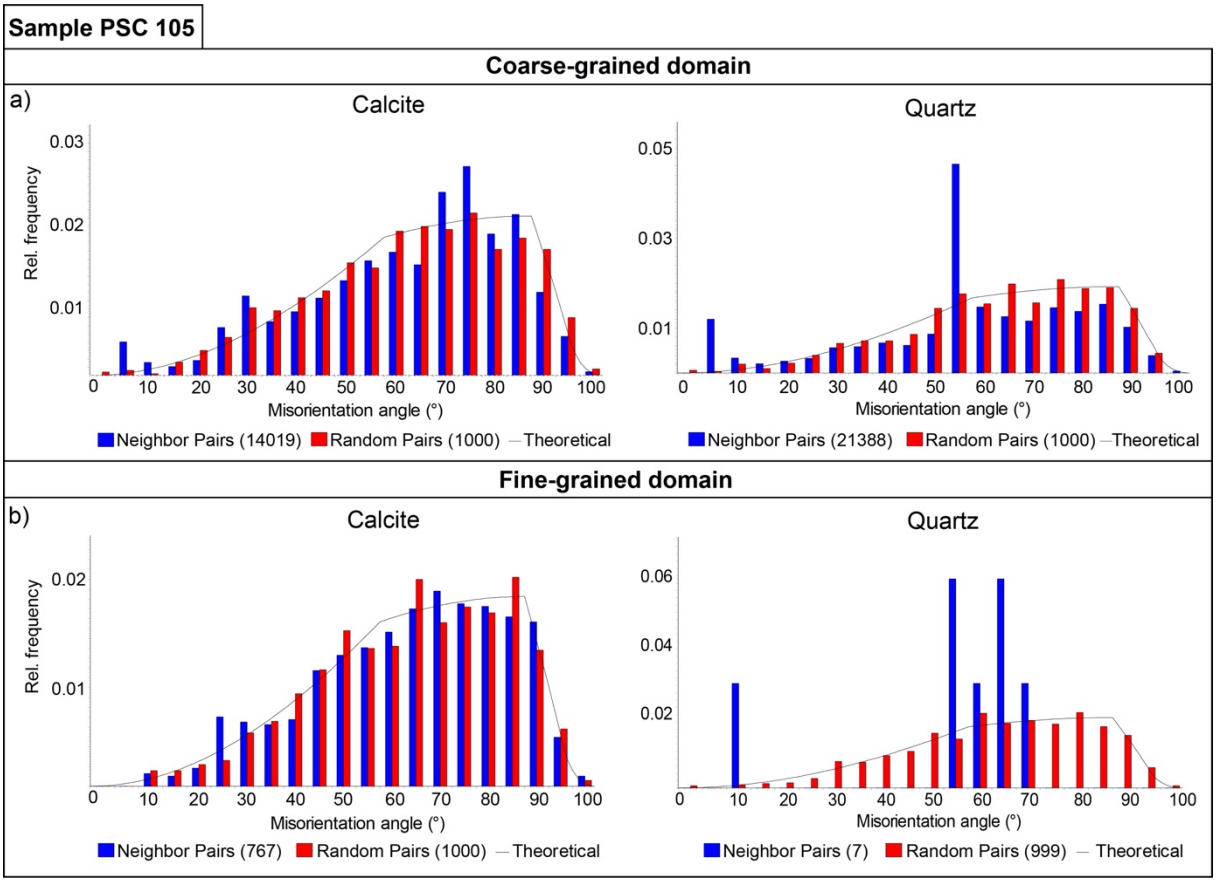

Figure 12: Distribution of misorientation angles for calcite and quartz. (a) Coarse-grained and; (b) Fine-grained domains of sample PSC 105

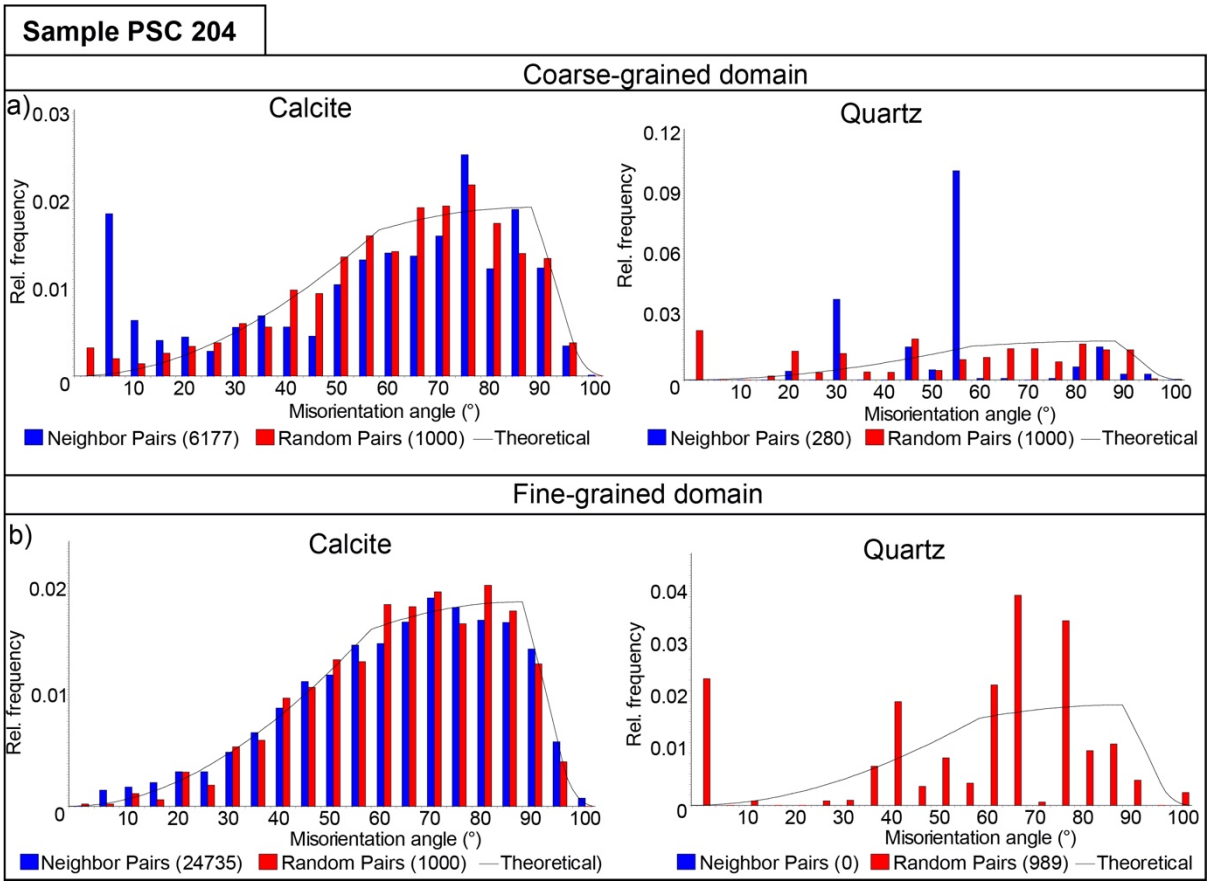

Figure 13: Distribution of misorientation angles for calcite and quartz. (a) Coarse-grained and; (b) Fine-grained domains of sample PSC 204.

QUARTZITE					
Mineral	**J-index**	**M-index**	**Sample**	**Deformation Mechanism**	**Slip System**
Quartz	1.05	0.003	PSC 003	Dissolution-precipitation creep	—
COARSE-GRAINED DOMAIN (METACARBONATE)					
Mineral	**J-index**	**M-index**	**Sample**	**Deformation Mechanism**	**Slip System**
Calcite	2.3	0.02	PSC 105	Dislocation creep/Dissolution-precipitation creep/ e-twinning	—
Calcite	2.2	0.08	PSC 204	Dislocation creep/Dissolution-precipitation creep	(c)<a>
Quartz	1.3	0.01	PSC 105	Oriented dissolution-precipitation creep	—
Quartz	1.3	0.03	PSC 204	Dissolution-precipitation creep	—
FINE-GRAINED DOMAIN (METACARBONATE)					
Mineral	**J-index**	**M-index**	**Sample**	**Deformation Mechanism**	**Slip System**
Calcite	1.1	0.01	PSC 105	Fluid-assisted grain boundary sliding	—
Calcite	1.3	0.01	PSC 204	Oriented dissolution-precipitation creep	—
Quartz	1.4	0.00	PSC 105	Fluid-assisted grain boundary sliding	—
Quartz	1.5	0.01	PSC 204	Fluid-assisted grain boundary sliding	—

97 **Table 1.** Representative deformation mechanisms determined for quartz and calcite in the
98 quartzite and metacarbonate samples from the study area.